

Spatiotemporal Pauli processes: Quantum combs for modelling correlated noise in quantum error correction

John F Kam^{1,2,3}, Angus Southwell¹, Spiro Gicev⁴, Muhammad Usman^{3,4}, and Kavan Modi⁵

¹School of Physics and Astronomy, Monash University, Clayton, VIC 3168, Australia

²Quantum Innovation Centre (Q.InC), Agency for Science Technology and Research (A*STAR), 2 Fusionopolis Way, Innovis #08-03, Singapore 138634, Republic of Singapore

³Quantum Systems, Data61, CSIRO, Clayton, VIC 3168, Australia

⁴School of Physics, The University of Melbourne, Parkville, VIC 3052, Australia

⁵Science, Mathematics and Technology Cluster, Singapore University of Technology and Design, 8 Somapah Road, 487372 Singapore

Correlated noise is a critical failure mode in quantum error correction (QEC), as temporal memory and spatial structure concentrate faults into error bursts that undermine standard threshold assumptions. Yet, a fundamental gap persists between the stochastic Pauli models ubiquitous in QEC and the microscopic, non-Markovian descriptions of physical device dynamics. We close this gap by introducing *Spatiotemporal Pauli Processes* (SPPs). By applying a multi-time Pauli twirl—operationally realised by Pauli-frame randomisation—to a general process tensor, we map arbitrary multi-time, non-Markovian dynamics to a multi-time Pauli process. This process is represented by a process-separable comb, or equivalently, a well-defined joint probability distribution over Pauli trajectories in spacetime. We show that SPPs inherit efficient tensor network representations whose bond dimensions are bounded by the environment’s Liouville-space dimension. To interpret these structures, we develop transfer operator diagnostics linking spectra to correlation decay, and exact hidden Markov representations for suitable classes of SPPs. We demonstrate the framework via surface code memory and stability simulations of up to distance 19 for (i) a temporally correlated “storm” model that tunes correlation length at fixed marginal error rates, and (ii) a genuinely spatiotemporal 2D quantum cellular automaton bath that maps exactly to a nonlinear probabilistic cellular automaton under twirling. Tuning coherent bath interactions drives the system into a pseudo-critical regime, exhibiting critical slowing down and macroscopic error avalanches that cause a complete breakdown of surface code distance scaling. Together, these results justify SPPs as an operationally grounded, scalable toolkit for modelling, diagnosing, and benchmarking correlated noise in QEC.

John F Kam: john.kam@monash.edu

Contents

1	Introduction	3
2	Background and formalism	6
2.1	Quantum channels and representations	6
2.2	Pauli channels and Pauli twirling	7
2.3	Pauli noise as an effective model for QEC	8
2.4	Process tensors and non-Markovianity	8
3	Process tensors as tensor networks	11
3.1	Stinespring-to-MPO construction	11
3.2	Higher-dimensional spatiotemporal tensor networks	14
4	Spatiotemporal Pauli processes	15
4.1	Multi-time Pauli twirling and SPPs	15
4.2	Local tensor network implementations	17
4.3	Worked examples: single-qubit non-Markovian dynamics	20
5	Characterising temporal correlations in 1D SPPs	23
5.1	Transfer operator framework	23
5.2	Spectral gap and correlation decay	25
5.3	Higher-dimensional generalisation	26
5.4	Equivalence to hidden Markov models	27
6	Surface code performance under temporal correlations	28
6.1	SPPs as effective circuit-level noise models	29
6.2	Temporal storm noise model	29
6.3	Simulation methodology	31
6.4	Surface code memory and stability benchmarks	32
7	Spatiotemporal noise via a quantum cellular automaton	33
7.1	Microscopic QCA dynamics	34
7.2	Effective probabilistic cellular automaton	36
7.3	Criticality and spatiotemporal correlations	37
7.4	Surface code breakdown near pseudo-criticality	39
8	Discussion	40
A	Notation translation table	47
B	Proof of process-separability of SPPs	48
C	Derivation of QCA to PCA HMM mapping	49
C.1	Setting and assumptions	49
C.2	Environment re-classicalisation induced by system twirling	50
C.3	Derivation of the PCA kernel	51
C.4	Conditional system Pauli emission	53
C.5	Summary of full mapping	54

1 Introduction

Correlations are increasingly recognised as decisive failure modes in quantum error correction (QEC) [1, 2]. Even when *average* error rates lie below conventional thresholds, the physics of real devices permits multipoint temporal memory and spatial structure that can concentrate faults into bursts [3, 4, 5, 6, 7], induce heavy tails in syndrome statistics [8], and ultimately undermine the independence assumptions behind standard threshold theorems [9, 10, 11]. Yet the modelling tools on either side of the physics–QEC interface remain misaligned. That is, on one hand, stochastic Pauli models are the workhorse of QEC design and analysis—enabling the scalable simulation [12], decoding [13, 14], and threshold statements [15, 16] that have driven much recent progress—but typically impose near-independence and introduce correlations only through ad hoc extensions. On the other hand, microscopic open quantum systems theories capture coherent dynamics and non-Markovian memory [17, 18, 19], but are rarely available in a form directly compatible with circuit-level benchmarking at scale.

A natural starting point for describing general open system dynamics is the quantum *process tensor* [20, 19] (Fig. 1 top left). Conceptually, it is the multi-time generalisation of a quantum channel, and is represented as a *quantum comb* [21, 22, 23, 24, 25, 26]. It provides an operationally complete description of non-Markovian dynamics by encoding the joint statistics of the system’s response under arbitrary interventions at multiple times. It thereby captures the full temporal correlation structure induced by an environment with quantum memory, and versions of this object have been characterised experimentally on quantum hardware [27, 28, 29, 30].

For QEC applications [31], however, this generality exposes a clear tension between expressivity and tractability. Process tensors are intrinsically quantum, high-rank objects whose complexity scales exponentially with both time and system dimension. In contrast, scalable circuit-level simulation and decoding are typically built around stochastic Pauli models. While these models often suffice in stabiliser settings [32], they are usually taken to be independent and identically distributed (i.i.d.), and may therefore fail to capture the genuinely spatiotemporal correlations present in real hardware. What is needed is a principled intermediate description—rich enough to encapsulate genuine spatiotemporal correlations, yet structured enough to support scalable circuit-level simulation, inference, and benchmarking.

To bridge this divide, we introduce *Spatiotemporal Pauli Processes* (SPPs) (Fig. 1 top right): stochastic processes over Pauli trajectories obtained by applying a *multi-time Pauli twirl* to a general process tensor (Fig. 1 top centre). Crucially, this projection is operationally motivated: it formalises the effective noise model induced by Pauli-frame randomisation [33, 34] and related randomised compiling techniques [35, 36, 37, 38]. Viewing the multi-time Pauli twirl as a *superprocess*, our central conceptual result is that it maps any (possibly non-Markovian) quantum process to a *process-separable* Pauli comb—equivalently, a well-defined joint probability distribution over Pauli trajectories across space and time. In this sense, SPPs are the natural multi-time analog of Pauli channels. This provides an operationally grounded noise framework compatible with both microscopic open systems modelling and the stabiliser workflow of QEC design and analysis.

We go beyond the operational definition, and show that SPPs admit efficient tensor network representations that can be constructed directly from an underlying system–environment interaction (Fig. 1 centre). Because the multi-time Pauli twirl acts strictly via local contractions on the system legs, the induced SPP inherits a classical tensor network form—whose entries encode joint spatiotemporal Pauli trajectory probabilities. Moreover,

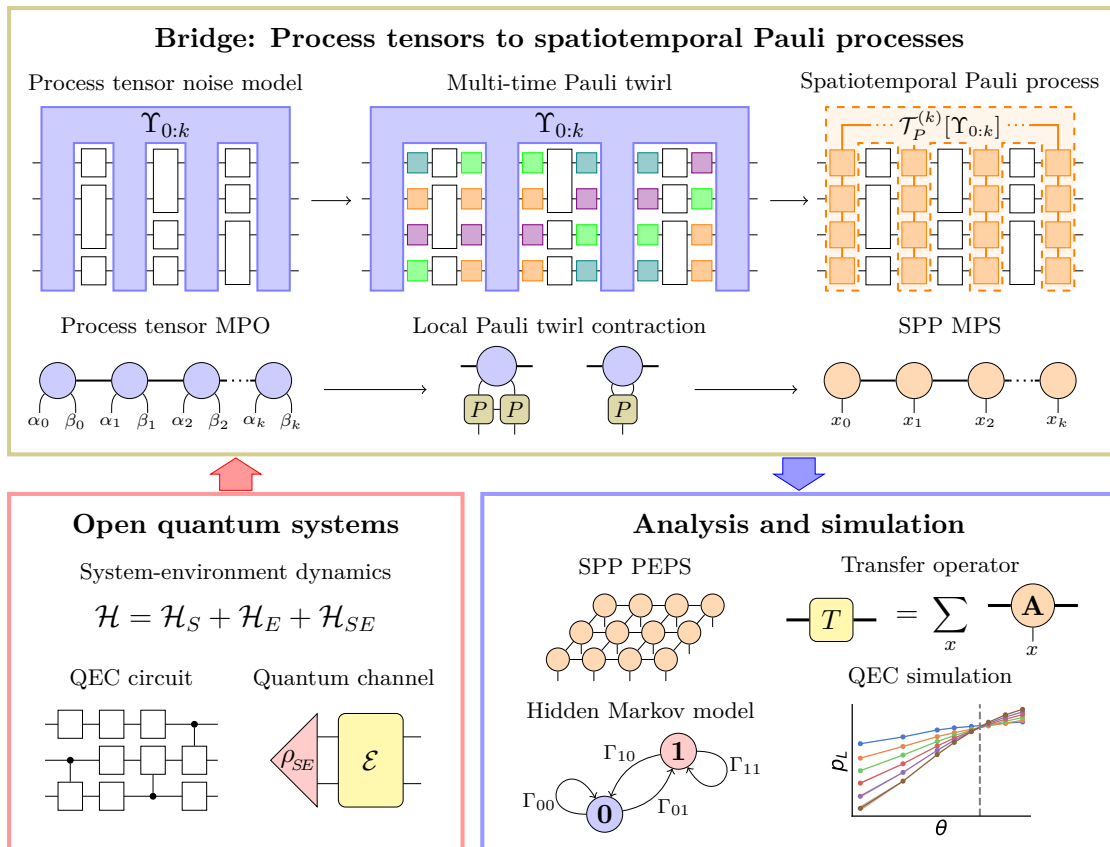


Figure 1: Framework overview: Process tensors to spatiotemporal Pauli processes. Starting from microscopic open quantum system dynamics (bottom left), we represent a process tensor description of noise and its tensor network form (top left). Applying the multi-time Pauli twirl (top centre)—as induced operationally by Pauli-frame randomisation—projects $\Upsilon_{0:k}$ onto a *spatiotemporal Pauli process* (SPP) (top right), i.e., a joint distribution over Pauli trajectories with a classical tensor network representation. The resulting SPP admits scalable analysis and simulation tools (bottom right), including transfer operator correlation diagnostics, hidden Markov model realisations, and Monte Carlo sampling for QEC benchmarking.

the inner bond dimension of this network is bounded by the Liouville-space [39] dimension of the underlying environment, tying the effective memory of the Pauli process to the size of the physical bath. To make these correlations interpretable, we develop a transfer operator formalism for SPPs that links spectral properties to temporal correlation lengths, and demonstrate that for suitable classes of SPPs, these tensor networks can be recast exactly to classical hidden Markov models. Together, these structures support efficient Monte Carlo sampling and inference, providing a direct interface between microscopic non-Markovian dynamics and circuit-level QEC simulation (Fig. 1 bottom right).

We deploy this framework to systematically benchmark primitives of surface code computation—including memory and stability—under correlated noise, simulating code distances up to 19. First, using a one-dimensional temporal “storm” model, we demonstrate that tuning the correlation length—while fixing single-round marginal error rates—progressively degrades logical memory and stability, blunting the effective exponential suppression of errors expected from distance scaling. Second, we introduce a genuinely spatiotemporal SPP derived from a two-dimensional coherent quantum cellular automaton (QCA) [40, 41] bath. Under operational Pauli twirling, the QCA dynamics maps to an

effective SPP described exactly by a probabilistic cellular automaton (PCA) with a non-linear transition kernel. Strikingly, tuning a single parameter controlling coherent bath interactions drives the Pauli process into a pseudo-critical regime. In this window, macroscopic error avalanches and critical slowing down cause a complete reversal and breakdown of standard surface code distance scaling. These results establish a concrete, computationally tractable link between non-equilibrium statistical mechanics and QEC performance under spatiotemporally correlated noise.

Our framework unifies three distinct domains: (i) higher-order quantum maps (process tensors) as a fully general language for multi-time open system dynamics; (ii) Pauli-frame randomisation and related compiling techniques that tailor physical noise into effective Pauli descriptions; and (iii) circuit-level QEC benchmarking workflows that demand scalable sampling and decoding.

Closely related reductions where Pauli twirling suppresses genuinely quantum non-Markovianity have also been identified in other formalisms. Liu *et al.* [42] derived an analogous statement for superchannels by twirling the associated ‘‘Choi-channel’’ representation, with related effects demonstrated experimentally in noise mitigation settings [43]. In contrast, we establish this reduction directly within the process tensor framework, rigorously generalising it to arbitrary multi-time, yielding a constructive tensor network-bridge, from microscopic system-environment dynamics to scalable correlated Pauli simulation and QEC benchmarking. Furthermore, a related, but conceptually distinct line of work has investigated the *single-snapshot* non-Markovianity of Pauli and Pauli-twirled channels via CP divisibility and embeddability criteria [44, 45]. This channel-level notion concerns the generator structure of an individual effective channel, whereas our framework treats non-Markovianity as an explicitly multi-time property of general quantum combs.

We now summarise the main contributions of this work below.

1. **Formalisation of spatiotemporal Pauli processes.** Spatiotemporal Pauli processes (SPPs) are defined as the multi-time Pauli-twirled image of a general process tensor, yielding a joint distribution over spatiotemporal Pauli trajectories.
2. **Constructive tensor-network representation with physical memory bounds.** SPP trajectory probabilities admit classical tensor network constructions via local Pauli-twirl contractions on process tensor network forms, with internal bond dimensions bounded by the environment Liouville dimension.
3. **Correlation diagnostics via transfer operators and HMM realisations.** Transfer operator spectra quantify correlation times, and suitable SPP tensor networks admit finite latent-state (hidden Markov) realisations for efficient sampling and inference.
4. **Controlled benchmarking under temporal correlations.** A tunable ‘‘storm’’ model family isolates the impact of temporal memory by varying correlation time at fixed single-round marginals in surface code memory and stability experiments.
5. **Distance-scaling breakdown from pseudo-critical QCA dynamics.** A microscopic 2D QCA bath induces an effective PCA SPP with pseudo-critical slowing down and avalanche-like errors, leading to a sharp breakdown of surface-code distance scaling.

The remainder of this paper is structured as follows. [Section 2](#) reviews background on quantum channels, Pauli twirling, and process tensors. [Section 3](#) constructs tensor-network representations of multi-time processes from microscopic dynamics. [Section 4](#) introduces SPPs via the multi-time Pauli twirl and derives their tensor network structure, with worked

examples. [Section 5](#) develops the transfer operator formalism and the connection to hidden Markov models. [Section 6](#) benchmarks surface code memory and stability under the temporally correlated storm model. [Section 7](#) derives an effective PCA from a coherent quantum bath and analyses the resulting pseudo-critical breakdown of distance scaling. Finally, [Section 8](#) concludes and discusses future applications.

2 Background and formalism

In this section, we establish the requisite machinery for our spatiotemporal Pauli process framework. We begin by reviewing quantum channels and their representations, then focus on Pauli channels and Pauli twirling, motivating their central role in quantum error correction while discussing their limitations. Finally, we generalise from two-time maps to multi-time dynamics via the process tensor formalism, which provides a rigorous description of non-Markovian memory and sets the stage for our later analysis of spatiotemporal noise correlations.

2.1 Quantum channels and representations

The physical evolution of a quantum state $\rho \in \mathcal{B}(\mathcal{H})$, where $\mathcal{B}(\mathcal{H})$ is the space of bounded linear operators on a Hilbert space \mathcal{H} , is entirely described by a *quantum channel* [46]. A quantum channel is a linear map $\mathcal{E} : \mathcal{B}(\mathcal{H}_{\text{in}}) \rightarrow \mathcal{B}(\mathcal{H}_{\text{out}})$ that is completely positive and trace preserving (CPTP). Formally, a quantum channel \mathcal{E} must satisfy:

1. **Linearity:** $\mathcal{E}[\alpha\rho_1 + \beta\rho_2] = \alpha\mathcal{E}[\rho_1] + \beta\mathcal{E}[\rho_2]$.
2. **Complete positivity (CP):** $(\mathcal{I}_A \otimes \mathcal{E}_B)[\rho_{AB}] \geq 0 \quad \forall \rho_{AB} \geq 0$.
3. **Trace preservation (TP):** $\text{Tr}(\mathcal{E}[\rho]) = \text{Tr}(\rho)$.

Physically, a channel represents a *two-time* quantum map evolving an initial state $\rho(t_0)$ at time t_0 to a final state $\rho(t_1)$ at time t_1 . A quantum channel admits several equivalent representations, each useful in different contexts. The most well-known representation is the Kraus (operator-sum) representation, which expresses the channel's action on an input state ρ as

$$\mathcal{E}[\rho] = \sum_i K_i \rho K_i^\dagger, \quad (1)$$

where the Kraus operators $\{K_i\}$ satisfy $\sum_i K_i^\dagger K_i = \mathbb{I}$ to ensure trace preservation. Another important representation is provided by the Choi-Jamiołkowski isomorphism (CJI), which establishes a bijection between CP maps $\mathcal{E} : \mathcal{B}(\mathcal{H}_{\text{in}}) \rightarrow \mathcal{B}(\mathcal{H}_{\text{out}})$ and positive semidefinite operators $\Upsilon \in \mathcal{B}(\mathcal{H}_{\text{in}} \otimes \mathcal{H}_{\text{out}})$. The Choi operator Υ is defined as

$$\Upsilon = (\mathcal{I} \otimes \mathcal{E})[|\Phi^+\rangle\langle\Phi^+|], \quad (2)$$

where $|\Phi^+\rangle = \sum_i |i\rangle \otimes |i\rangle$ is the (unnormalised) Bell state on $\mathcal{H}_{\text{in}} \otimes \mathcal{H}_{\text{in}}$. The action of the Choi operator Υ on an input state ρ can then be written as

$$\mathcal{E}[\rho] = \text{Tr}_{\text{in}}[(\rho^T \otimes \mathbb{I}_{\text{out}})\Upsilon]. \quad (3)$$

The CP condition on \mathcal{E} translates into the positive semidefiniteness of Υ , while the TP condition translates to the partial trace relation $\text{Tr}_{\text{out}}[\Upsilon] = \mathbb{I}_{\text{in}}$. This representation directly encodes the complete dynamical information of a channel into a static bipartite state.

This duality is generalised to later multi-time processes described by process tensors in [Section 2.4](#).

The Stinespring dilation theorem provides an additional, physically motivated perspective on quantum channels. It states that any CPTP map acting on a system space $\mathcal{B}(\mathcal{H}_S)$ can be realised as a unitary operation U on a larger, dilated space $\mathcal{B}(\mathcal{H}_S \otimes \mathcal{H}_E)$, followed by a partial trace over an auxiliary environment E . This is expressed as

$$\mathcal{E}[\rho_S] = \text{Tr}_E[U(\rho_S \otimes \sigma_E)U^\dagger], \quad (4)$$

where σ_E is an initial state of the environment, which must be initially separable from ρ_S .

Throughout this work, we also employ further representations, including the χ -matrix¹ representation and the (Liouville-)superoperator representation. The χ -matrix is related to the Choi matrix via a change of basis to the Pauli basis, while the superoperator representation is convenient for numerical calculations. We do not explicitly review these representations nor the detailed mappings between them. For a comprehensive overview of quantum channel representations and the transformations between them in a graphical calculus, we refer the reader to Ref. [\[39\]](#).

2.2 Pauli channels and Pauli twirling

An important class of quantum channels, especially in quantum error correction, is the class of Pauli channels [\[46\]](#). A Pauli channel \mathcal{E}_P acting on n qubits is defined as a convex mixture of Pauli operators,

$$\mathcal{E}_P[\rho] = \sum_{P \in \mathbb{P}^{(n)}} p_P P \rho P, \quad (5)$$

where $\mathbb{P}^{(n)} = \{I, X, Y, Z\}^{\otimes n}$ is the n -qubit Pauli basis, and coefficients $p_P \geq 0$ satisfy $\sum_P p_P = 1$.

Any general channel \mathcal{E} can be projected into a Pauli channel via a procedure known as *Pauli twirling*. The Pauli twirl of \mathcal{E} is defined as the group average

$$\mathcal{T}_P(\mathcal{E})[\rho] = \frac{1}{|\mathbb{P}^{(n)}|} \sum_{P \in \mathbb{P}^{(n)}} P \mathcal{E}(P \rho P) P, \quad (6)$$

where $|\mathbb{P}^{(n)}| = 4^n$. The image of the twirling operation is strictly a Pauli channel of the form in [Eq. \(5\)](#). Equivalently, given the χ -matrix representation of \mathcal{E} , the twirled channel $\mathcal{T}_P(\mathcal{E})$ can be computed by zeroing all off-diagonal elements, leaving only the diagonal elements corresponding to probabilities p_P of the Pauli operators. In the Choi representation, the twirling operation acts as a CPTP *projector* (an idempotent and hermiticity-preserving map) on the Choi operator Υ :

$$\mathcal{T}_P(\Upsilon) = \frac{1}{4^n} \sum_{P \in \mathbb{P}^{(n)}} (P \otimes P) \Upsilon (P \otimes P). \quad (7)$$

This operation removes coherences between different Pauli operators (off-diagonal elements in the χ -matrix) while preserving the CPTP condition. Pauli twirling can therefore be viewed as a *supermap* [\[21\]](#)—a higher-order quantum operation—as it maps valid quantum channels to valid quantum channels. We will later generalise this projection in the process tensor framework. Before turning to multi-time processes, however, we first discuss the relevance and limitations of Pauli noise models in quantum error correction.

¹Also known as a process matrix, a term we avoid using due to a terminological clash with the higher-order quantum object with potentially indefinite causal order [\[23\]](#).

2.3 Pauli noise as an effective model for QEC

Pauli noise models occupy a privileged role in quantum error correction. The discretisation of errors via projective syndrome measurements collapses continuous error processes into discrete outcomes associated with Pauli errors—allowing the correction of general noise [47, 32]. Furthermore, via the Gottesman-Knill theorem [48], Clifford circuits subject to Pauli noise are amenable to efficient classical simulation, enabling large-scale Monte Carlo studies of QEC performance in regimes relevant for fault-tolerant computation [49, 12].

Physical noise processes, however, are described by general CPTP maps that need not be Pauli channels [46]. Coherent unitary errors—arising from miscalibrated gates, drift, or unwanted system-system or system-environment couplings—induce structure in noise that is explicitly discarded by the Pauli twirling approximation. Consequently, stochastic Pauli models cannot wholly capture the full underlying dynamics and can, in some cases, mispredict logical error rates, as seen in worst-case analyses with highly coherent gate-based noise [50, 51]. These discrepancies are further exacerbated in non-Markovian settings [31], where coherent environmental memory effects defy characterisation even by sequences of general quantum channels.

Despite these limitations, there are compelling reasons to treat Pauli noise as a central effective noise model for QEC. First and foremost, Pauli twirling can be engineered in practice. Randomised compiling (RC) actively tailors general noise into stochastic Pauli noise on the physical level by interleaving and compiling random Pauli gates into the circuit [35, 37, 38]. Second, many of the most dramatic examples where Pauli models misdiagnose logical failure rates rely on highly structured and fully coherent error patterns that are unlikely to persist in large-scale devices [50]. QEC performance under less pathological non-Pauli models, such as amplitude or phase damping, is well approximated by their Pauli twirled counterparts [52, 53]. Furthermore, previous studies suggest that residual coherent effects on logical qubits are naturally suppressed with increasing code distance for standard stabiliser codes [54, 55].

Finally, the efficiency of Pauli noise representations enables a range of practical noise characterisation protocols. In particular, the reconstruction of effective phenomenological Pauli noise from syndrome measurement data alone [56, 57, 58] is highly valuable for in situ monitoring and calibration of real-world QEC implementations [59].

Crucially, even with a Pauli description of noise, one can still accommodate the rich, albeit, spatiotemporal correlations induced by non-Markovian dynamics. Most existing analyses, however, assume uncorrelated, Markovian error models, whereas correlations in stochastic models can have a pronounced impact on the efficacy of QEC protocols [60, 2].

This motivates the central arc of the paper: We begin from a fully general, multi-time description of noise, and then construct an operational bridge to the Pauli-fault language used by stabiliser-based QEC. In the next subsection, we introduce the process tensor formalism, which provides a complete description of multi-time quantum processes—including non-Markovian memory effects—and serves as the starting point of our construction. We then develop tensor network representations of process tensors in Section 3, which are essential for deriving the efficient spatiotemporal Pauli descriptions in Sections 4 and 5.

2.4 Process tensors and non-Markovianity

While quantum channels describe two-time dynamics, they are insufficient for capturing general multi-time quantum processes, especially in the presence of non-Markovian memory effects. The quantum *process tensor* provides a general spatiotemporal framework that encodes all such correlations. It can be viewed as a *higher-order quantum map* (or quantum

comb), that takes as input a sequence of k instruments $\mathbf{A}_{0:k-1} = (\mathcal{A}_0, \dots, \mathcal{A}_{k-1})$, and outputs the resulting system state ρ_{out} . Here each \mathcal{A}_j denotes a CP map acting on the system at time t_j , representing an arbitrary control operation, gate, or projective measurement performed by an experimenter. Additionally, what exactly constitutes an instrument can be defined contextually. For instance, relevant for QEC, a syndrome extraction cycle can be treated as a single instrument [61, 31]. The set of sequences $\{\mathbf{A}_{0:k-1}\}$ thus broadly encapsulates all possible controllable dynamics imposed on the system between the initial preparation and the final time.

For the purposes of modelling the multi-time dynamics starting from an initial system state ρ_{in} ², we define a k -slot process tensor $\mathcal{T}_{0:k}$ as a multilinear map acting on ρ_{in} and $\mathbf{A}_{0:k-1}$ by

$$\mathcal{T}_{0:k}[\rho_{\text{in}}, \mathbf{A}_{0:k-1}] = \rho_{\text{out}}. \quad (8)$$

Like quantum channels, a process tensor admits several equivalent representations, the most prevalent being the Choi representation. Just as the CJI establishes a channel-state duality, there exists a process-state duality that maps any quantum process $\mathcal{T}_{0:k}$ to a positive semidefinite operator $\Upsilon_{0:k} \in \mathcal{B}(\bigotimes_{j=0}^k \mathcal{H}_{\text{in}_j} \otimes \mathcal{H}_{\text{out}_j})$. Its action on an initial state ρ_{in} and sequence $\mathbf{A}_{0:k-1}$ is given by

$$\rho_{\text{out}}(\rho_{\text{in}}, \mathbf{A}_{0:k-1}) = \text{Tr}_{\text{out}} \left[\left(\rho_{\text{in}}^T \otimes \hat{\mathcal{A}}_0^T \otimes \dots \otimes \hat{\mathcal{A}}_{k-1}^T \otimes \mathbb{I}_{\text{out}} \right) \Upsilon_{0:k} \right], \quad (9)$$

where Tr_{out} denotes the partial trace over all subspaces except the final output space $\mathcal{H}_{\text{out}_k}$, and $\hat{\mathcal{A}}_j \in \mathcal{B}(\mathcal{H}_{\text{out}_j} \otimes \mathcal{H}_{\text{in}_{j+1}})$ is the Choi operator of the CP map \mathcal{A}_j . For $k = 0$, the above expression reduces to the channel case in Eq. (3).

Equivalent Kraus, superoperator, and χ -matrix representations can be derived from the Choi form in direct analogy with quantum channels. The Choi representation is convenient because it translates the physical properties of a quantum process into concrete properties of the operator $\Upsilon_{0:k}$. Crucially, a process tensor $\mathcal{T}_{0:k}$ represents a valid, physical process if and only if its Choi representation $\Upsilon_{0:k}$ satisfies the following conditions:

1. Multi-linearity

The Choi operator $\Upsilon_{0:k}$ represents a multilinear map $\mathcal{T}_{0:k}$ with respect to the input state ρ_{in} and each instrument in the instrument sequence $\mathbf{A}_{0:k-1}$,

$$\begin{aligned} \mathcal{T}_{0:k}[\alpha\rho_1 + \beta\rho_2, \mathbf{A}_{0:k-1}] &= \alpha\mathcal{T}_{0:k}[\rho_1, \mathbf{A}_{0:k-1}] + \beta\mathcal{T}_{0:k}[\rho_2, \mathbf{A}_{0:k-1}], \\ \mathcal{T}_{0:k}[\rho_{\text{in}}, \alpha\mathbf{A}_1 + \beta\mathbf{A}_2] &= \alpha\mathcal{T}_{0:k}[\rho_{\text{in}}, \mathbf{A}_1] + \beta\mathcal{T}_{0:k}[\rho_{\text{in}}, \mathbf{A}_2]. \end{aligned} \quad (10)$$

2. Positive semidefiniteness

This is the direct generalisation of the CP condition for quantum channels. The Choi operator must be positive semidefinite,

$$\Upsilon_{0:k} \geq 0, \quad (11)$$

ensuring that, for any valid initial state and sequence of instruments, the output state is positive semidefinite.

²For cases where the system and environment are initially correlated, the process tensor acts purely on a sequence of instruments $\mathbf{A}_{0:k-1}$, where the initial map \mathcal{A}_0 serves as a preparation map. Correspondingly, a *supermap* [21] is exactly a 1-slot process tensor in this definition.

3. Causal (or affine) constraints

Also known as the containment property, these constraints are a more intricate generalisation of the TP condition of channels to multi-time processes. The Choi operator must satisfy the recursive constraints,

$$\begin{aligned}\mathrm{Tr}_{\mathrm{out}_j}[\Upsilon_{0:j}] &= \Upsilon_{0:j-1} \otimes \mathbb{I}_{\mathrm{in}_j}, \quad \forall j = 1, \dots, k, \\ \mathrm{Tr}_{\mathrm{out}_0}[\Upsilon_{0:0}] &= \mathbb{I}_{\mathrm{in}_0}.\end{aligned}\tag{12}$$

Operationally, this condition ensures that instruments performed at future times cannot influence outcome statistics at earlier times, thereby enforcing causal ordering. Equivalently, these constraints can be expressed as a linear system of Pauli expectation values. Denoting

$$\langle P_{\mathrm{in}_0} P_{\mathrm{out}_0} \cdots P_{\mathrm{in}_k} P_{\mathrm{out}_k} \rangle = \mathrm{Tr}[(P_{\mathrm{in}_0} \otimes P_{\mathrm{out}_0} \otimes \cdots \otimes P_{\mathrm{in}_k} \otimes P_{\mathrm{out}_k}) \Upsilon_{0:k}],\tag{13}$$

with Pauli strings $P_j \in \mathbb{P}^{(n)}$ of cardinality $|\mathbb{P}^{(n)}| = 4^n$, and non-identity Pauli strings $Q_j \in \mathbb{P}^{(n)} \setminus \{\mathbb{I}\}$, Eq. (12) can be rewritten as $(k+1)(4^n - 1)$ independent linear equations,

$$\begin{aligned}\langle P_{\mathrm{in}_0} P_{\mathrm{out}_0} \cdots P_{\mathrm{out}_{k-1}} Q_{\mathrm{in}_k} \mathbb{I}_{\mathrm{out}_k} \rangle &= 0, \\ \langle P_{\mathrm{in}_0} P_{\mathrm{out}_0} \cdots P_{\mathrm{out}_{k-2}} Q_{\mathrm{in}_{k-1}} \mathbb{I}_{\mathrm{out}_{k-1}} \mathbb{I}_{\mathrm{in}_k} \mathbb{I}_{\mathrm{out}_k} \rangle &= 0, \\ &\vdots \\ \langle Q_{\mathrm{in}_0} \mathbb{I}_{\mathrm{out}_0} \cdots \mathbb{I}_{\mathrm{in}_k} \mathbb{I}_{\mathrm{out}_k} \rangle &= 0.\end{aligned}\tag{14}$$

The normalisation condition $\langle \mathbb{I}_{\mathrm{in}_0} \mathbb{I}_{\mathrm{out}_0} \cdots \mathbb{I}_{\mathrm{in}_k} \mathbb{I}_{\mathrm{out}_k} \rangle = \mathrm{Tr}[\Upsilon_{0:k}] = 4^{n(k+1)}$ provides an additional linear constraint, however it is often convenient to work with the unnormalised Choi state.

In summary, the set of Choi states representing physical quantum processes $\{\Upsilon_{0:k}\}$ lies in the intersection of the convex cone of positive semidefinite operators and an affine subspace defined by the causal constraints on the process tensor.

Beyond these general validity conditions, structural features of a process tensor reflect the physical nature of the underlying dynamics. Notably, entanglement across temporal partitions of a Choi state $\Upsilon_{0:k}$ —referred to as *temporal entanglement*—signals that a process is *genuinely quantum non-Markovian*. Concretely, a process exhibits genuinely quantum temporal correlations if and only if its Choi state cannot be written as a convex mixture of products,

$$\Upsilon_{0:k} = \sum_{\vec{\alpha}=(\alpha_0, \alpha_1, \dots, \alpha_k)} p_{\vec{\alpha}} \Upsilon_0^{\alpha_0} \otimes \Upsilon_1^{\alpha_1} \otimes \cdots \otimes \Upsilon_k^{\alpha_k},\tag{15}$$

with $p_{\alpha} \geq 0$ and each Υ_j^{α} is the Choi representation of a CPTP channel. Processes that can be written in this form are *process-separable*, possessing temporal correlations that are classically simulable. Conversely, a process is fully *Markovian*—exhibiting neither quantum nor classical temporal correlations—if and only if its Choi operator factorises across all time steps,

$$\Upsilon_{0:k}^{\mathrm{Markov}} = \Upsilon_0 \otimes \Upsilon_1 \otimes \cdots \otimes \Upsilon_k,\tag{16}$$

where each Υ_j is CPTP. The dynamics of a Markovian process is therefore equivalently generated by a sequence of independent quantum channels.

The physical origin of these structures can be traced back to the system-environment picture. By a natural extension of the Stinespring dilation theorem, any k -slot process

tensor can be realised as the joint multi-time dynamics of a system S and an environment E , followed by a partial trace over the environment. This is represented by the equation,

$$\mathcal{T}_{0:k}[\rho_S, \mathbf{A}_{0:k-1}] = \text{Tr}_E [\mathcal{U}_k \circ \mathcal{A}_{k-1} \circ \mathcal{U}_{k-1} \circ \cdots \circ \mathcal{A}_0 \circ \mathcal{U}_0(\sigma_E \otimes \rho_S)], \quad (17)$$

where $\mathcal{U}(\cdot) = U(\cdot)U^\dagger$ implements a joint system-environment unitary, $\mathbf{A}_{0:k-1}$ is a sequence of CP maps acting only on S , and we have assumed an initially separable system and environment state $\sigma_E \otimes \rho_S$.

This dilation is more than a mathematical device; it depicts the fundamental physics governing open quantum dynamics. Non-Markovianity arises when the environment retains information about the system's past and feeds it back into its future evolution. What is precisely considered an environment can be broadly interpreted as any inaccessible (or ignored) degrees of freedom that influences the system's evolution. In the QEC context, this could include spurious two-level systems, higher energy levels of transmons, cosmic ray-induced phonons, or even other neighbouring qubits when considering reduced subsystem dynamics.

Chiefly, the process tensor formalism abstracts away the explicit modelling of the environment. Instead, it centralises the environment's *influence* on the system with respect to all possible interventions by an experimenter.

In the next section, we exploit this structure to construct tensor network representations of process tensors, which serve as the foundation of our spatiotemporal Pauli process framework.

3 Process tensors as tensor networks

Quantum maps are tensors; when correlations between their indices are even modestly constrained, they often admit compact tensor network representations. A paradigmatic example is the matrix product state (MPS) description of quantum many-body states with area-law entanglement. The same principle extends to quantum processes: process tensors are high-rank objects whose temporal correlations are often structured, making tensor network representations both natural and efficient [62]. Accordingly, process tensors have been represented as matrix product operators (MPOs) [20, 63], locally purified density operators (LPDOs) [25], and tree tensor networks (TTNs) [64].

In what follows, we construct tensor network representations of process tensors directly from their microscopic dynamics. We begin with a one-dimensional temporal MPO obtained from a Stinespring dilation, before generalising to higher-dimensional spatiotemporal tensor networks for composite systems. Throughout, we employ abstract index notation supplemented by a graphical tensor network calculus. A table translating primitives of quantum information in Dirac notation, abstract indices, and graphical diagrams is provided in [Section A](#).

3.1 Stinespring-to-MPO construction

We begin by constructing an MPO representation of a process tensor from its Stinespring dilation. A k -slot process tensor is fully specified by a sequence of joint system-environment unitaries $\{U_j\}_{j=0}^k$ together with an initial environment state σ_E . In general, one may start from a sequence of joint CPTP maps $\{\mathcal{E}_j\}_{j=0}^k$, which, by Stinespring's theorem can always be dilated to unitaries.

For a unitary U acting on $\mathcal{H}_E \otimes \mathcal{H}_S$ of dimensions d_E and d_S , its Liouville (superoperator) form is $\mathcal{U} = \bar{U} \otimes U$, where $\bar{U} = U^*$ denotes elementwise complex conjugation. In

index notation,

$$\mathcal{U}^{e'_0 s'_0 e_0 s_0}_{e'_i s'_i e_i s_i} = \overline{U}^{e'_0 s'_0}_{e'_i s'_i} U^{e_0 s_0}_{e_i s_i}, \quad (18)$$

where e_i, s_i (e_0, s_0) label environment and system input (output) indices, and primed indices mark dual ‘bra’ spaces, with unprimed indices denoting vector ket spaces. To make the connection between the Stinespring dilation and tensor networks transparent, we introduce a specialised tensor representation derived from the Liouville form via a *reorder–fuse–transpose* (RFT) operation:

1. **Reorder** indices to group each ket index with its corresponding bra index.
2. **Fuse** each bra–ket (primed–unprimed) pair into a single compound index.
3. **Transpose** globally so that time flows from left to right, consistent with standard circuit diagrams.

Explicitly, for a superoperator \mathcal{S} ,

$$\begin{aligned} & \mathcal{S}^{b'_0 b'_1 \dots b_0 b_1}_{a'_0 a'_1 \dots a_0 a_1} \\ & \xrightarrow{\text{reorder}} \mathcal{S}^{b'_0 b_0 b'_1 b_1 \dots}_{a'_0 a_0 a'_1 a_1 \dots} \xrightarrow{\text{fuse}} \mathcal{S}^{\beta_0 \beta_1 \dots}_{\alpha_0 \alpha_1 \dots} \xrightarrow{\text{transpose}} \mathbf{S}^{\alpha_0 \alpha_1 \dots}_{\beta_0 \beta_1 \dots}, \end{aligned} \quad (19)$$

where $\alpha_j = (a'_j a_j)$ and $\beta_j = (b'_j b_j)$ are fused indices of dimension $\dim(\alpha_j) = \dim(a_j)^2$. Latin letters denote basic indices and Greek letters fused indices. The RFT mapping simply re-expresses a superoperator as a tensor network-friendly object whose left–right orientation matches the temporal ordering of the process. This form is convenient for both graphical calculus and numerical implementations, where each fused index corresponds to the vectorised operator space of a particular physical subsystem.

Applying the RFT operation to a unitary superoperator \mathcal{U}_j yields a 4-legged tensor $\mathbf{U}_{(j)}$,

$$\mathcal{U}_j^{e'_{j+1} e_{j+1} b'_j b_j}_{e'_j e_j a'_j a_j} \xrightarrow{\text{RFT}} \mathbf{U}_{(j)}^{\mu_j \alpha_j}_{\mu_{j+1} \beta_j}, \quad (20)$$

with fused indices $\mu_j = (e'_j e_j)$ for the environment and $\alpha_j = (a'_j a_j)$, $\beta_j = (b'_j b_j)$ for the system input and output, respectively. Their dimensions are $\dim(\mu_j) = d_E^2$ and $\dim(\alpha_j) = \dim(\beta_j) = d_S^2$. The mapping is graphically depicted as

$$\begin{aligned} & \begin{array}{c} \mu_j \text{---} \text{---} \mu_{j+1} \\ \alpha_j \text{---} \text{---} \beta_j \end{array} \mathbf{U}_{(j)} \\ & = \left(\begin{array}{c} e'_{j+1} \text{---} \text{---} e'_j \\ e_{j+1} \text{---} \text{---} e_j \\ b'_j \text{---} \text{---} a'_j \\ b_j \text{---} \text{---} a_j \end{array} \begin{array}{c} \overline{U}_j \\ U_j \end{array} \right)^T, \end{aligned} \quad (21)$$

where thick wires represent fused indices. The initial environment state $|\sigma_E\rangle\rangle$ is mapped similarly,

$$\sigma^{e'_0 e_0} \xrightarrow{\text{RFT}} \sigma_{\mu_0} \longleftrightarrow \left\langle \sigma \right| \mu_0 = \left(\begin{array}{c} e'_0 \text{---} \text{---} e'_0 \\ e_0 \text{---} \text{---} e_0 \end{array} \sigma_E \right)^T, \quad (22)$$

where we have adopted the column-stacking convention for vectorisation. To represent the final partial trace over the environment, we include a trace tensor \mathbf{t} , corresponding to the unnormalised Bell state $|\Phi^+\rangle = |\mathbb{I}\rangle\rangle$,

$$\mathbf{t}^{\mu_{k+1}} = \delta^{e'_{k+1} e_{k+1}} \longleftrightarrow \mu_{k+1} \text{---} \text{---} \text{---} = \begin{array}{c} e'_{k+1} \text{---} \text{---} \\ \text{---} \text{---} \\ e_{k+1} \text{---} \text{---} \end{array}. \quad (23)$$

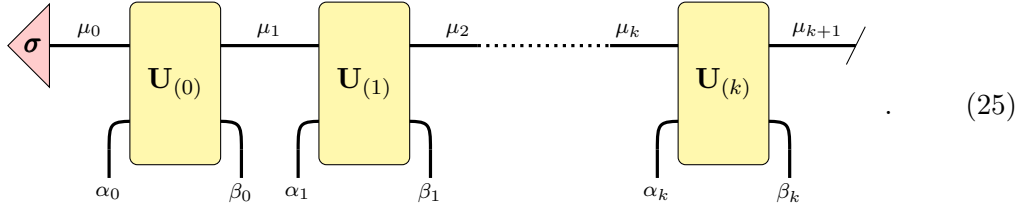
The full k -slot process tensor is then constructed as an MPO by contracting the environment indices μ_j across all time. This yields a tensor \mathbf{T} with open system indices corresponding to the inputs (α_j) and outputs (β_j) at each time j . We formalise this in the following definition.

Definition 3.1 (MPO representation of a process tensor). A k -slot process tensor $\Upsilon_{0:k}$ admits a matrix product operator (MPO) representation,

$$\mathbf{T}^{\alpha_0, \dots, \alpha_k}_{\beta_0, \dots, \beta_k} = \sum_{\mu_0, \dots, \mu_{k+1}} \boldsymbol{\sigma}_{\mu_0} \mathbf{U}_{(0)}^{\mu_0 \alpha_0}_{\mu_1 \beta_0} \mathbf{U}_{(1)}^{\mu_1 \alpha_1}_{\mu_2 \beta_1} \cdots \mathbf{U}_{(k)}^{\mu_k \alpha_k}_{\mu_{k+1} \beta_k} \mathbf{t}^{\mu_{k+1}}. \quad (24)$$

Here $\boldsymbol{\sigma}$, $\mathbf{U}_{(j)}$, and \mathbf{t} are tensor representations of the initial environment state, the joint SE unitary at time j , and the final environment trace, respectively. The environment indices μ_j are the MPO's virtual bonds of dimension $D = \dim(\mu_j) \leq d_E^2$, corresponding to the dimension of the environment's Liouville space.

In graphical form,



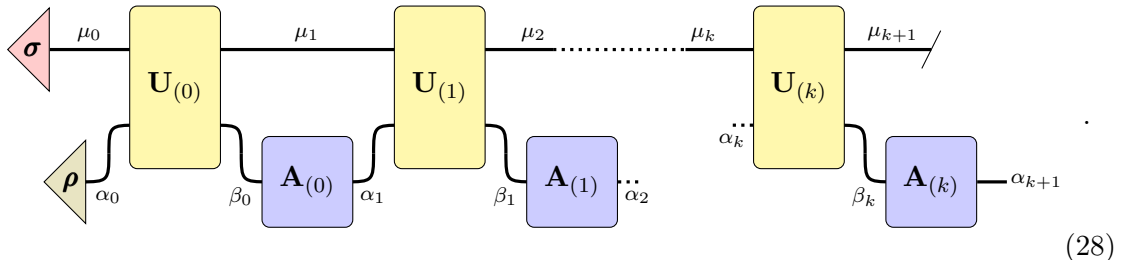
To recover the standard Choi form, we simply reorder and reshape the fused indices as

$$\mathbf{T}^{\alpha_0, \dots, \alpha_k}_{\beta_0, \dots, \beta_k} \mapsto \mathbf{T}_{\text{Choi}}^{a_0 b_0 \dots a_k b_k}_{a'_0 b'_0 \dots a'_k b'_k} \longleftrightarrow \Upsilon_{0:k}. \quad (26)$$

In the tensor network picture, the action of \mathbf{T} on an initial state and sequence of instruments is realised as a network contraction between the ‘top comb’ process tensor and the ‘bottom comb’ sequence of instruments. The initial system state $|\rho_{\text{in}}\rangle\rangle$ and each instrument superoperator \mathcal{A}_j are mapped into their corresponding tensors $\boldsymbol{\rho}^{\text{in}}$ and $\mathbf{A}_{(j)}$ via the RFT operation. The final output state $\boldsymbol{\rho}^{\text{out}}$ is then given by

$$\boldsymbol{\rho}_{\alpha_{k+1}}^{\text{out}} = \boldsymbol{\sigma}_{\mu_0} \boldsymbol{\rho}_{\alpha_0}^{\text{in}} \mathbf{U}_{(0)}^{\mu_0 \alpha_0}_{\mu_1 \beta_0} \mathbf{A}_{(0) \alpha_1}^{\beta_0} \mathbf{U}_{(1)}^{\mu_1 \alpha_1}_{\mu_2 \beta_1} \mathbf{A}_{(1) \alpha_2}^{\beta_1} \cdots \mathbf{U}_{(k)}^{\mu_k \alpha_k}_{\mu_{k+1} \beta_k} \mathbf{t}^{\mu_{k+1}} \mathbf{A}_{(k) \alpha_{k+1}}^{\beta_k}, \quad (27)$$

where repeated indices imply summation (contraction). Graphically, the output state ρ_{out} is described by



This contraction naturally generalises to cases where the instruments are themselves classically or ‘quantumly’ correlated in time, in which case the product of local instrument tensors is replaced by a more general tensor network. Having established a 1D temporal MPO representation of multi-time processes, we now lift this construction to composite systems with additional spatial structure.

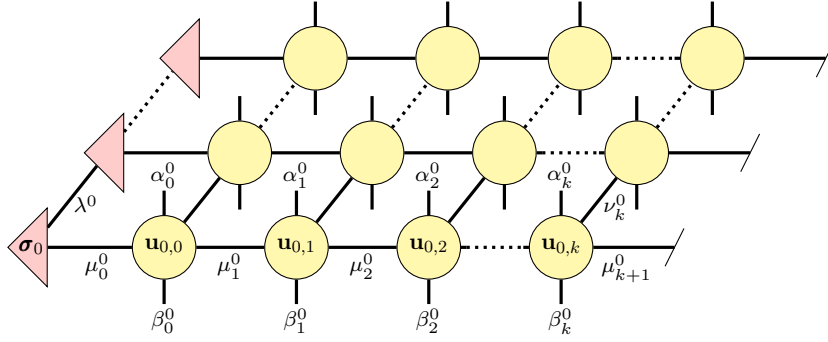


Figure 2: Spatiotemporal tensor network form of a process tensor. Horizontal bonds μ_j^i encode temporal correlations, bonds ν_j^i carry spatial correlations, and open indices α_j^i , β_j^i correspond to system inputs and outputs at each time $j \in [0, k]$ and subsystem $i \in [0, n]$.

3.2 Higher-dimensional spatiotemporal tensor networks

So far we have considered only the one-dimensional temporal structure of process tensors, where each tensor carries dense system indices of size d_S^2 . For composite systems—such as spin chains—these indices can be further factorised along spatial degrees of freedom, promoting the MPO to a two-dimensional tensor network with time along one axis and space along the other. Concretely, we decompose the system legs of each temporal tensor into local legs associated with individual subsystems. For a unitary tensor $\mathbf{U}_{(j)}$ acting on an n -partite system, we can perform a series of singular value decompositions (SVDs) along subsystem indices, yielding

$$\mathbf{U}_{(j)}^{\mu_j^0 \alpha_j}{}_{\mu_{j+1} \beta_j} = \sum_{\nu_j^0, \dots, \nu_j^{n-2}} \mathbf{u}_{(0,j)}^{\mu_j^0 \alpha_j^0}{}_{\beta_j^0 \mu_{j+1}^0 \nu_j^0} \mathbf{u}_{(1,j)}^{\nu_j^0 \mu_j^0 \alpha_j^1}{}_{\beta_j^1 \mu_{j+1}^1 \nu_j^1} \dots \mathbf{u}_{(n-1,j)}^{\nu_j^{n-2} \mu_j^{n-1} \alpha_j^{n-1}}{}_{\beta_j^{n-1} \mu_{j+1}^{n-1}}. \quad (29)$$

Here the superscript $i = 0, \dots, n-1$ labels subsystems (spatial coordinates), and ν_j^i are newly introduced bond indices that link neighbouring subsystems at each time t_j . The environment-induced temporal bonds μ_j^i remain on each subsystem line. Performing this decomposition for all j and similarly for the initial environment tensor $\boldsymbol{\sigma}$, we obtain a 2D tensor network representation of the process tensor,

$$\mathbf{T}^{\{\alpha_j^i\}}{}_{\{\beta_j^i\}} = \sum_{\{\mu_j^i\}} \sum_{\{\lambda^i\}} \sum_{\{\nu_j^i\}} \left[\prod_{i=0}^{n-1} \boldsymbol{\sigma}^{\lambda^{i-1}}{}_{\mu_0^i \lambda^i} \right] \left[\prod_{j=0}^k \prod_{i=0}^{n-1} \mathbf{u}_{(i,j)}^{\nu_j^{i-1} \mu_j^i \alpha_j^i}{}_{\beta_j^i \mu_{j+1}^i \nu_j^i} \right] \left[\prod_{i=0}^{n-1} \mathbf{t}_{(i)}^{\mu_{k+1}^i} \right], \quad (30)$$

with spatial boundary conditions such that left indices λ^{-1} , ν_j^{-1} and right indices λ^{n-1} , ν_j^{n-1} are absent. In this representation, horizontal bonds μ_j^i carry temporal correlations (environmental memory), while vertical bonds ν_j^i encode spatial correlations between subsystems at each time step. The spatial bond dimensions $D_s = \dim(\nu_j^i)$ are set by the SVD truncation, while the temporal bond dimensions remain bounded by the environment size, $D_t = \dim(\mu_j^i) \leq d_E^2$. Figure 2 displays a graphical representation of this 2D tensor network.

Unlike the 1D temporal MPO representation, 2D tensor networks are generally not both exactly and efficiently contractible. In practice one must resort to approximate contraction schemes, whose cost is controlled by the entanglement across the chosen contraction direction. For spatiotemporal processes, however, the causal structure along the time dimension

imposes additional constraints on the allowed correlations, which can often be exploited by tailored contraction algorithms [65, 62].

The above construction also extends straightforwardly to higher spatial dimensions by allowing each time slice to be represented by a higher-dimensional tensor network—for example, a 2D projected entangled pair operator (PEPO) for a planar system. Moreover, while we derived the higher-dimensional network by factorising the temporal MPO into spatial components, one may instead construct a tensor network reflecting the microscopic system–environment dynamics, especially when the interactions are local [25, 31]. This flexibility allows for efficient constructions tailored to the specific spatiotemporal structure of the underlying process.

4 Spatiotemporal Pauli processes

We now introduce *spatiotemporal Pauli processes* (SPPs), the effective stochastic processes induced by applying the *multi-time Pauli twirl* to a quantum process tensor. The twirl maps an arbitrary (possibly non-Markovian) process to a joint distribution over spatiotemporal Pauli trajectories, eliminating genuinely quantum temporal correlations while retaining arbitrary classical correlations. Crucially, in a tensor-network representation this map is implemented by fixed local contractions on the physical legs at each time step, leaving the virtual (environment) bonds unchanged. This yields an explicit classical tensor network—an MPS in 1D and a PEPS in 2D—encoding the trajectory weights (and hence probabilities). As a direct consequence, the temporal bond dimensions of the resulting SPP tensor networks are bounded by the corresponding process tensor bonds, and in particular by the environment Liouville dimension d_E^2 for finite environments. These results justify SPPs as a natural tensor-network-compatible description of correlated circuit-level Pauli noise, and provide the technical foundation for the explicit noise models and QEC studies developed in later sections.

4.1 Multi-time Pauli twirling and SPPs

We begin by extending the standard Pauli twirling operation for quantum channels to multi-time processes.

Let $\mathbb{P}^{(n)}$ denote the n -qubit Pauli group modulo global phase. Define

$$\mathcal{H}_{\Upsilon_{0:k}} := \bigotimes_{j=0}^k (\mathcal{H}_{i_j} \otimes \mathcal{H}_{o_j}), \quad (31)$$

and let $\Upsilon_{0:k} \in \mathcal{B}(\mathcal{H}_{\Upsilon_{0:k}})$ be the Choi operator representation of a k -slot process tensor.

Definition 4.1 (Multi-time Pauli twirl). The multi-time Pauli twirl $\mathcal{T}_P^{(k)}$ is the CPTP projector

$$\mathcal{T}_P^{(k)}(\Upsilon_{0:k}) = \frac{1}{|\mathbb{P}^{(n)}|^{k+1}} \sum_{P_0, \dots, P_k \in \mathbb{P}^{(n)}} \left(\bigotimes_{j=0}^k P_j \otimes P_j \right) \Upsilon_{0:k} \left(\bigotimes_{j=0}^k P_j \otimes P_j \right). \quad (32)$$

Intuitively, $\mathcal{T}_P^{(k)}$ independently twirls each time step’s input-output pair on $\mathcal{H}_{i_j} \otimes \mathcal{H}_{o_j}$, preserving the causal structure of the process tensor. In the language of higher-order quantum maps [26], the multi-time Pauli twirl constitutes a time-local *superprocess*, since

it maps physical processes to physical processes. Operationally, it corresponds to Pauli-frame randomisation protocols [66]; standard randomised compiling provides one such implementation.

We now summarise the key properties of this mapping.

Proposition 4.2 (Properties). The map $\mathcal{T}_P^{(k)}$ satisfies the following properties:

1. **Validity:** For any CPTP process tensor $\Upsilon_{0:k}$, its twirl $\mathcal{T}_P^{(k)}(\Upsilon_{0:k})$ is also a CPTP process tensor.
2. **Projector:** $\mathcal{T}_P^{(k)}$ is idempotent, $\mathcal{T}_P^{(k)} \circ \mathcal{T}_P^{(k)} = \mathcal{T}_P^{(k)}$.
3. **Causality:** The affine (causal) constraints are preserved under twirling.

The first two properties generalise those of standard Pauli twirling for quantum channels, while the third follows from the unitality of Pauli operators ($\mathcal{T}_P^{(k)}[\mathbb{I}] = \mathbb{I}$ on each local pair). We now demonstrate that this projection removes all quantum temporal correlations, yielding a process-separable object corresponding to a probability distribution over Pauli trajectories.

Let $\mathcal{P} = (P_0, P_1, \dots, P_k)$ denote a *spatiotemporal Pauli trajectory*, where each $P_j \in \mathbb{P}^{(n)}$ is an n -qubit Pauli operator at time step t_j , and $\Pi_{P_j} = |P_j\rangle\rangle\langle\langle P_j|$ its corresponding Pauli Choi operator. Let $\mathbb{P}^{(n,k)}$ denote the set of all such spatiotemporal Pauli trajectories over $k+1$ time steps, and let $\Pr(\mathcal{P})$ denote the trajectory weights induced by the twirl, defined explicitly in Eq. (35).

Theorem 4.3 (Twirling yields a process-separable Pauli process). *For any process tensor $\Upsilon_{0:k}$, its twirl*

$$\Upsilon_{0:k}^{\mathcal{T}_P} := \mathcal{T}_P^{(k)}(\Upsilon_{0:k}) \quad (33)$$

admits a process-separable decomposition

$$\Upsilon_{0:k}^{\mathcal{T}_P} = \sum_{\mathcal{P} \in \mathbb{P}^{(n,k)}} \Pr(\mathcal{P}) \Upsilon_{\mathcal{P}}, \quad \Upsilon_{\mathcal{P}} = \bigotimes_{j=0}^k \Pi_{P_j}. \quad (34)$$

Probabilities $\Pr(\mathcal{P})$ form a valid probability distribution given by

$$\Pr(\mathcal{P}) = \frac{w(\mathcal{P})}{\mathcal{N}}, \quad w(\mathcal{P}) := \text{Tr} \left[\left(\bigotimes_{j=0}^k \Pi_{P_j} \right) \Upsilon_{0:k} \right] \geq 0, \quad \mathcal{N} := \sum_{\mathcal{P} \in \mathbb{P}^{(n,k)}} w(\mathcal{P}). \quad (35)$$

The resulting twirled process tensor $\Upsilon_{0:k}^{\mathcal{T}_P}$ is *process-separable* in the sense of Eq. (15), i.e., it is a convex mixture of temporally factorised Pauli Choi operators. Equivalently, the twirl removes all genuinely quantum temporal correlations while allowing arbitrary classical temporal correlations through the joint distribution $\Pr(\mathcal{P})$. A detailed proof is provided in Section B.

We now formalise this class of process-separable objects under the name *spatiotemporal Pauli process*.

Definition 4.4 (Spatiotemporal Pauli process). A *spatiotemporal Pauli process* (SPP) is a process tensor with Choi representation

$$\Upsilon_{\text{SPP}} = \sum_{\mathcal{P} \in \mathbb{P}^{(n,k)}} \Pr_{\text{SPP}}(\mathcal{P}) \Upsilon_{\mathcal{P}}, \quad \Upsilon_{\mathcal{P}} = \bigotimes_{j=0}^k \Pi_{P_j}, \quad (36)$$

where $\Pr_{\text{SPP}}(\mathcal{P})$ is a probability distribution with $\Pr_{\text{SPP}}(\mathcal{P}) \geq 0$ and $\sum_{\mathcal{P}} \Pr_{\text{SPP}}(\mathcal{P}) = 1$.

In the special case of a fully temporally independent SPP—containing neither classical nor quantum temporal correlations—the trajectory probabilities factorise as

$$\Pr_{\text{SPP}}(P_0, \dots, P_k) = \prod_{j=0}^k \Pr_j(P_j). \quad (37)$$

As a result, the Choi operator $\Upsilon_{\text{SPP}}^{\text{Markov}}$ factorises as in Eq. (16), corresponding to a sequence of temporally independent Pauli channels.

The multi-time Pauli twirl should be interpreted operationally. It does not assert the microscopic system–environment dynamics are physically transformed into a process-separable Pauli process. Rather, under the assumed randomisation protocol (e.g., randomised compiling or Pauli-frame randomisation), it yields an effective description that reproduces the Pauli-basis statistics of the original dynamics. This is particularly potent for applications such as in QEC. For example, in the context of a QEC circuit, Υ_{SPP} can be interpreted as the effective, generally correlated, circuit-level Pauli noise model obtained by applying the multi-time twirl to the original noisy circuit.

The reduction of non-Markovian dynamics to classical temporal correlations under Pauli twirling has also been recently identified in different formalisms. Liu et al. [42] derived an analogous result for single-slot superchannels by applying standard channel twirling to the associated “Choi channel” representation. A closely related statement was also obtained and demonstrated experimentally in the context of a noise mitigation protocol [43]. In contrast, our derivation establishes this reduction directly within the process tensor framework and rigorously generalises it to arbitrary multi-time processes.

While SPPs can be defined directly via Theorem 4.4 without reference to an underlying quantum process, our formulation using the multi-time twirl provides a direct bridge between the physically grounded system–environment dynamics and the emergent stochastic Pauli process. This connection endows SPPs with the same rich internal structure as process tensors, enabling a straightforward and efficient tensor network construction. In particular, we show that $\mathcal{T}_P^{(k)}$ is implemented by fixed local contractions on the physical legs of the process tensor.

4.2 Local tensor network implementations

We now show that the multi-time Pauli twirl admits an exact local implementation on a process tensor network. Concretely, $\mathcal{T}_P^{(k)}$ is realised by inserting a fixed Pauli tensor on each system input–output leg at every time step. This produces (i) a twirled process tensor MPO in the operator picture, and (ii) a classical tensor encoding the joint weights (and hence probabilities) of Pauli trajectories. Centrally, this transformation acts only on the open physical indices and leaves inner (environment) bonds unchanged.

Starting from the Pauli superoperator $P^* \otimes P$, we define the Pauli tensor \mathbf{P} via the reorder–fuse–transpose (RFT) operation introduced in Section 3 as

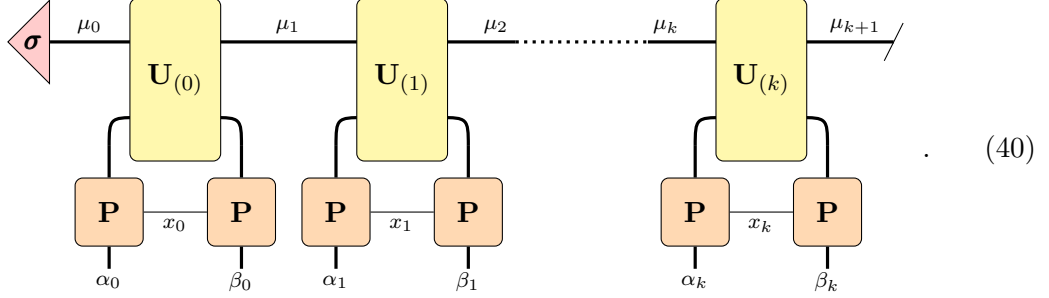
$$\overline{P}_{(x)a'}^{b'} P_{(x)a}^b \xrightarrow{\text{RFT}} \mathbf{P}^{\alpha}_{\beta x} \quad \longleftrightarrow \quad \begin{array}{c} \alpha \text{---} \boxed{\mathbf{P}} \text{---} \beta \\ | \\ x \end{array} \equiv \begin{array}{c} \alpha \quad \beta \\ | \quad | \\ \triangle \mathbf{P} \\ | \\ x \end{array}, \quad (38)$$

where the index x of $\dim x = 4^n$ enumerates the n -qubit Pauli operators.

Proposition 4.5 (Local tensor network implementation of the multi-time Pauli twirl). Let \mathbf{T} be a tensor network (MPO) representation of a k -slot process tensor as in Eq. (24). Then the multi-time Pauli twirl $\tilde{\mathbf{T}} := \mathcal{T}_P^{(k)}(\mathbf{T})$ is obtained by contracting a pair of the Pauli tensor \mathbf{P} with each open system index pair (α_j, β_j) at every time step as

$$\tilde{\mathbf{T}}^{\alpha_0 \dots \alpha_k \beta_0 \dots \beta_k} = \mathbf{T}^{\alpha'_0 \dots \alpha'_k \beta'_0 \dots \beta'_k} \left(\prod_{j=0}^k \mathbf{P}^{\alpha'_j \alpha_j}_{x_j} \mathbf{P}^{\beta'_j \beta_j}_{x_j} \right), \quad (39)$$

where primed indices are summed over. Graphically,



In particular, this operation implements the twirl locally on the physical legs and leaves the environment bonds μ_j unchanged. This is a direct rewriting of Theorem 4.1 in the Pauli Liouville basis using \mathbf{P} and the RFT re-indexing in Eq. (19). The resulting tensor $\tilde{\mathbf{T}}$ is related to the standard Choi representation of the twirled process tensor via Eq. (26).

The local contraction in Theorem 4.5 also gives direct access to the (unnormalised) trajectory weights by contracting only one Pauli tensor per time step into the open legs of the untwirled tensor network. Let $\mathbf{x}_{0:k} = (x_0, x_1, \dots, x_k)$ index a spatiotemporal Pauli trajectory, where each x_j labels an n -qubit Pauli operator. The trajectory weights are defined as

$$\mathbf{w}_{x_0 \dots x_k} := \mathbf{T}^{\alpha_0 \dots \alpha_k \beta_0 \dots \beta_k} \prod_{j=0}^k \mathbf{P}^{\alpha_j \beta_j}_{x_j}, \quad (41)$$

and the corresponding normalised probabilities

$$\Pr(\mathbf{x}_{0:k}) = \mathbf{p}_{x_0 \dots x_k} := \frac{\mathbf{w}_{x_0 \dots x_k}}{\mathcal{N}}, \quad \mathcal{N} := \sum_{x_0 \dots x_k} \mathbf{w}_{x_0 \dots x_k}. \quad (42)$$

This reproduces Eq. (35) under the identification $x_j \leftrightarrow P_j$.

Although $\mathbf{w}_{x_0 \dots x_k}$ is an exponentially large tensor, it inherits an efficient MPS form from the process tensor MPO for which we can directly construct its local tensors.

Definition 4.6 (Process tensor MPO to SPP MPS). Given a process tensor \mathbf{T} with Stinespring dilation $\{\mathbf{U}_{(j)}, \boldsymbol{\sigma}\}$, the spatiotemporal Pauli process obtained by multi-time twirling admits an MPS representation with tensors

$$\begin{aligned} \mathbf{A}_{x_0 \mu_1} &= \boldsymbol{\sigma}_{\mu_0} \mathbf{U}^{\mu_0 \alpha_0}_{\mu_1 \beta_0} \mathbf{P}^{\alpha_0}_{\beta_0 x_0} \\ \mathbf{A}^{\mu_j}_{x_j \mu_{j+1}} &= \mathbf{U}^{\mu_j \alpha_j}_{\mu_{j+1} \beta_j} \mathbf{P}^{\alpha_j}_{\beta_j x_j} \\ \mathbf{A}^{\mu_k}_{x_k} &= \mathbf{U}^{\mu_k \alpha_k}_{\mu_{k+1} \beta_k} \mathbf{t}^{\mu_{k+1}} \mathbf{P}^{\alpha_k}_{\beta_k x_k}, \end{aligned} \quad (43)$$

where the initial environment tensor $\boldsymbol{\sigma}$ and the final trace \mathbf{t} have been absorbed into the boundary tensors. The resulting MPS,

$$\mathbf{w}_{x_0 \dots x_k} = \mathbf{A}_{x_0 \mu_1} \left(\prod_{j=1}^{k-1} \mathbf{A}^{\mu_j}_{x_j \mu_{j+1}} \right) \mathbf{A}^{\mu_k}_{x_k}, \quad (44)$$

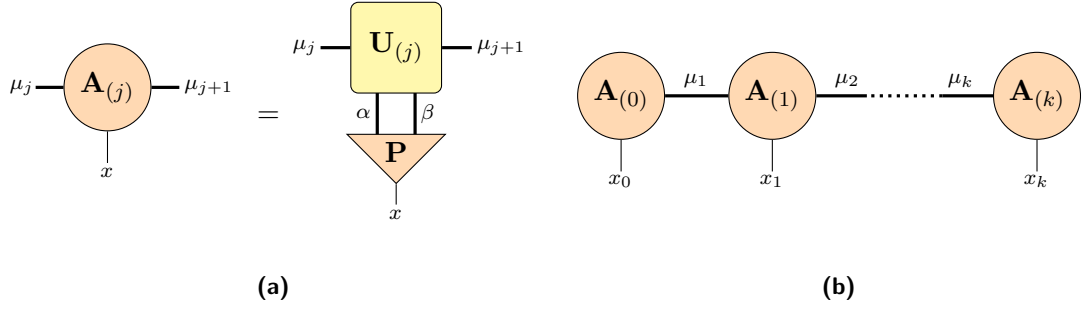


Figure 3: 1D SPP as an MPS over Pauli trajectories. (a) Local tensor obtained by contracting the system–environment unitary tensor $\mathbf{U}^{(j)}$ with the Pauli tensor \mathbf{P} , corresponding to a local Pauli twirl on the system. (b) Resulting matrix product state (MPS) representation of the SPP trajectory weights, where environment bonds μ_j mediate temporal correlations and physical indices x_j label Pauli outcomes at each time step. Sampling this MPS yields Pauli trajectories $\mathbf{x}_{0:k}$ with probability $\Pr(\mathbf{x}_{0:k})$.

encodes the (unnormalised) joint probability distribution over Pauli trajectories, denoting the exact probability tensor $\mathbf{p}_{x_0\dots x_k} := \Pr(\mathbf{x}_{0:k}) = \mathbf{w}_{x_0\dots x_k}/\mathcal{N}$.

Importantly, [Theorem 4.5](#) and [Theorem 4.6](#) show that the map from a process tensor MPO to the SPP MPS acts only on the physical indices and leaves the environment bonds μ_j unchanged. This immediately implies that the temporal bond dimension required to represent the induced SPP cannot increase.

Lemma 4.7 (Bond dimension bound for SPP MPS). *Let \mathbf{T} be a process tensor admitting an MPO form whose inner bond dimensions are $\dim \mu_j$ for each time step t_j . The resulting SPP MPS encoding the joint probability distribution $\Pr(\mathbf{x}_{0:k})$, defined in [Theorem 4.4](#), admits an MPS representation with inner bond dimensions D_j satisfying*

$$D_j \leq \dim \mu_j \quad \forall j. \quad (45)$$

Proof. The tensors of the SPP MPS are obtained by applying a local, linear map to the physical indices of the process tensor MPO tensors. This operation acts strictly on the system Hilbert space and leaves the environment bonds μ_j invariant. Since the minimum required bond dimension D_j is determined by the Schmidt rank across the temporal partition, and no operations are performed on the virtual bonds, the rank cannot increase. Therefore, the bond dimension is strictly bounded by the dimension of the original virtual space, $D_j \leq \dim \mu_j$. \square

Corollary 4.8 (Environment dimension bound). *For a process derived from a system interacting with a finite environment of dimension d_E , the inner bond dimensions of the resulting SPP MPS is bounded by the Liouville space dimension of the environment,*

$$D_j \leq d_E^2. \quad (46)$$

For generic Haar-random system–environment unitaries, the bound in [Theorem 4.7](#) is typically saturated (up to finite-size effects), since the induced temporal memory explores the full environment Liouville space.

This construction, illustrated in [Fig. 3](#), provides a direct method for sampling Pauli trajectories from the joint distribution using standard MPS sampling algorithms. Conversely, if the operator description is required, the twirled process tensor MPO $\tilde{\mathbf{T}}$ can be

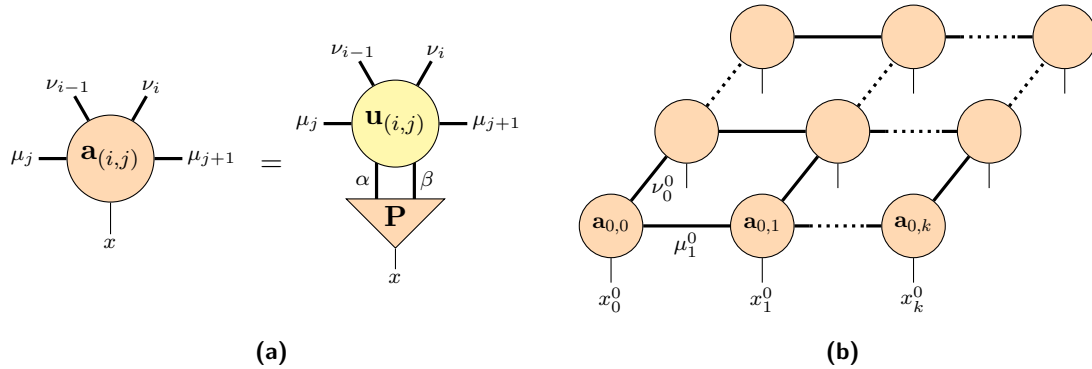


Figure 4: 2D SPP as a PEPS over spatiotemporal Pauli faults. (a) Local tensor transformation for 2D tensor network representation. (b) Projected entangled-pair state (PEPS) representation of the SPP trajectory weights. Spatial correlations are encoded along one axis by bonds ν_j^i , while temporal correlations are encoded along the other axis by bonds μ_j^i .

perfectly recovered from the SPP MPS by re-expanding the Pauli basis indices x_j as

$$\tilde{\mathbf{T}}^{\alpha_0 \dots \alpha_k}_{\beta_0 \dots \beta_k} = \mathbf{p}_{x_0 \dots x_k} \left(\prod_{j=0}^k \mathbf{P}^{x_j \alpha_j}_{\beta_j} \right). \quad (47)$$

Equations (41), (42) and (47) hence provide two equivalent descriptions of the induced SPP: as a Pauli-diagonal MPO $\tilde{\mathbf{T}}$ in the operator picture, and as a classical MPS \mathbf{p} encoding $\Pr(x_{0:k})$.

Finally, nothing in the above construction relies on a one-dimensional (MPS/MPO) geometry. The multi-time Pauli twirl is implemented by inserting the same fixed Pauli tensor \mathcal{P} on the open indices. Consequently, for any process tensor represented by a tensor network—for instance, a tree tensor network or a higher-dimensional PEPO—the twirl produces a tensor network encoding the classical joint trajectory weights. To illustrate the 2D case, the multi-time Pauli twirl maps the process tensor PEPO to a projected entangled pair state (PEPS) representation of the SPP. The constituent tensors of this PEPS network are given by

$$\mathbf{a}_{(i,j)}^{\nu_j^{i-1} \mu_j^i}_{x_j^i \mu_{j+1}^i \nu_j^i} = \mathbf{u}_{(i,j)}^{\nu_j^{i-1} \mu_j^i \alpha_j^i}_{\beta_j^i \mu_{j+1}^i \nu_j^i} \mathbf{P}^{\beta_j^i}_{\alpha_j^i x_j^i}, \quad (48)$$

As shown in Fig. 4, spatial correlations are encoded along the bonds ν_j^i , while temporal correlations remain encoded along the bonds μ_j^i . The bond dimension bound of Theorem 4.7 applies individually to each temporal bond in the PEPS network. We next illustrate the SPP framework by introducing three simple system-environment Hamiltonians and explicitly computing the corresponding single-slot (two time slices) SPPs.

4.3 Worked examples: single-qubit non-Markovian dynamics

Consider a single system qubit S coupled to a single environment qubit E , with joint Hilbert space $\mathcal{H}_S \otimes \mathcal{H}_E$. We study three families of system-environment Hamiltonians $H(\theta) \in \mathcal{B}(\mathcal{H}_S \otimes \mathcal{H}_E)$, generating unitary dynamics of the form

$$U(\theta) = e^{-iH(\theta)}, \quad (49)$$

where θ is a tunable parameter. Concretely, we consider:

1. **Heisenberg interaction:** $H_J(\theta_J) = -\frac{1}{2}\theta_J(X^S \otimes X^E + Y^S \otimes Y^E + Z^S \otimes Z^E)$
Generates exchange interactions; in particular, $U_J(\pi/2)$ is equivalent to a SWAP operator up to a global phase. This is a paradigmatic model for non-Markovian dynamics and is known to generate strong temporal correlations.
2. **Controlled- X rotation:** $H_{RX}(\theta_{RX}) = -\frac{1}{2}\theta_{RX}(X^S \otimes I^E - X^S \otimes Z^E)$
Generates a controlled rotation on the system along the X -axis, with the environment acting as the control. At $\theta_{RX} = \pi/2$, the resulting unitary is equivalent to a CNOT gate up to a global phase.
3. **Heisenberg with local field:** $H_F(\theta_F) = H_J(\frac{\pi}{2}) - \theta_F(X^S + Y^S + Z^S) \otimes I^E$
A maximal exchange Heisenberg interaction modulated by a local field on the system, breaking the symmetry of the pure Heisenberg model.

Given $U(\theta)$ and choosing an initial environment state $\rho_E = |+\rangle\langle+|$, we construct the corresponding single-slot (two time slices) process tensor $\Upsilon_{0:1}(\theta)$ in the standard Choi representation using Eqs. (24) and (26). We then apply the multi-time Pauli twirl in Eq. (32) to obtain the corresponding SPP $\Upsilon_{0:1}^{\mathcal{T}_P}(\theta)$.

To study how these processes transform under twirling, we compute measures of temporal correlations alongside Pauli trajectory probabilities. A key diagnostic is the *generalised quantum mutual information* (GQMI), defined as the quantum relative entropy between the original process tensor $\Upsilon_{0:k}$ and the product of its single-time marginals

$$\Upsilon_{0:k}^{\text{Markov}} = \text{Tr}_{\bar{0}}[\Upsilon_{0:k}] \otimes \text{Tr}_{\bar{1}}[\Upsilon_{0:k}] \otimes \cdots \otimes \text{Tr}_{\bar{k}}[\Upsilon_{0:k}], \quad (50)$$

where $\text{Tr}_{\bar{j}}[\cdot]$ denotes the partial trace over all input-output spaces except those at time step t_j . The GQMI \mathcal{I} is then

$$\mathcal{I}[\Upsilon_{0:k}] = S(\Upsilon_{0:k} \| \Upsilon_{0:k}^{\text{Markov}}) = \text{Tr}[\Upsilon_{0:k}(\log \Upsilon_{0:k} - \log \Upsilon_{0:k}^{\text{Markov}})]. \quad (51)$$

In addition, we introduce a second quantity $\mathcal{J}[\Upsilon_{0:k}]$ based on the relative entropy between a process and its Pauli-twirled counterpart, quantifying the non-Pauli structure discarded by the multi-time twirl. Defining $\Upsilon_{0:k}^{\mathcal{T}_P} = \mathcal{T}_P^{(k)}(\Upsilon_{0:k})$, we set

$$\mathcal{J}[\Upsilon_{0:k}] = S(\Upsilon_{0:k} \| \Upsilon_{0:k}^{\mathcal{T}_P}). \quad (52)$$

By a property of the quantum relative entropy, $\mathcal{J}[\Upsilon_{0:k}] \geq 0 \forall \Upsilon_{0:k} \geq 0$, with equality if and only if $\Upsilon_{0:k} = \Upsilon_{0:k}^{\mathcal{T}_P}$; equivalently, the process is invariant under the multi-time twirl.

We evaluate $\mathcal{I}[\Upsilon_{0:1}]$, $\mathcal{I}[\Upsilon_{0:1}^{\mathcal{T}_P}]$, and $\mathcal{J}[\Upsilon_{0:1}]$ for each Hamiltonian family as functions of the interaction strength, where Choi operators $\Upsilon_{0:1}$ are normalised such that $\text{Tr}[\Upsilon_{0:1}] = 1$. Figure 5 plots each quantity over $\theta \in [0, 2\pi]$. For the Heisenberg model in panel (a), $\mathcal{I}[\Upsilon_{0:1}]$ is maximal at $\theta_J = (2n+1)\pi/2$, $n \in \mathbb{Z}$, corresponding to a SWAP-like operation, and minimal for $\theta_J = n\pi$, corresponding to the identity operation. Notably, the twirled process has $\mathcal{I}[\Upsilon_{0:1}^{\mathcal{T}_P}] = 0$ for all θ_J , that is, due to the symmetry of the interaction, the induced SPP is always temporally independent.

To visualise the Pauli sequence probabilities directly, Fig. 6 plots $\text{Pr}(\mathcal{P}_{0:1})$ at representative parameter values for each model. For the Heisenberg interaction at $\theta_J = (2n+1)\pi/2$ in panel (a), the resulting SPP is a uniform distribution over all 16 possible Pauli trajectories, corresponding to maximally depolarising noise at each step; correspondingly, $\mathcal{J}[\Upsilon_{0:1}]$ is maximal, indicating the original process is farthest from its twirled counterpart.

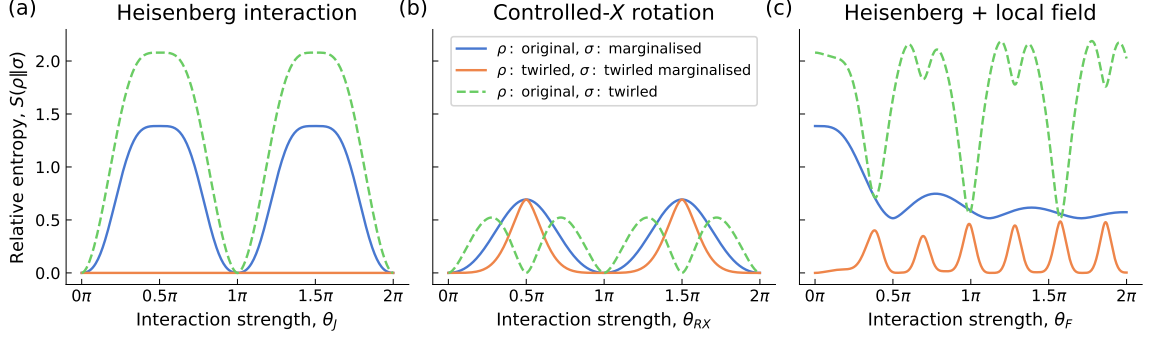


Figure 5: Quantum relative entropy diagnostics of SPPs. We plot the generalised quantum mutual information $\mathcal{I}[\Upsilon_{0:1}] = S(\Upsilon_{0:1} \| \Upsilon_{0:1}^{\text{Markov}})$, its twirled counterpart $\mathcal{I}[\Upsilon_{0:1}^{\mathcal{T}_P}]$, and the twirl relative entropy $\mathcal{J}[\Upsilon_{0:1}]$ as functions of interaction strength $\theta \in [0, 2\pi]$ for three different Hamiltonian families. Choi operators are normalised such that $\text{Tr}[\Upsilon_{0:1}] = 1$, and the environment is initialised in $|+\rangle$. Panels: (a) Heisenberg exchange interaction, (b) controlled- X rotation, (c) Heisenberg exchange with local field.

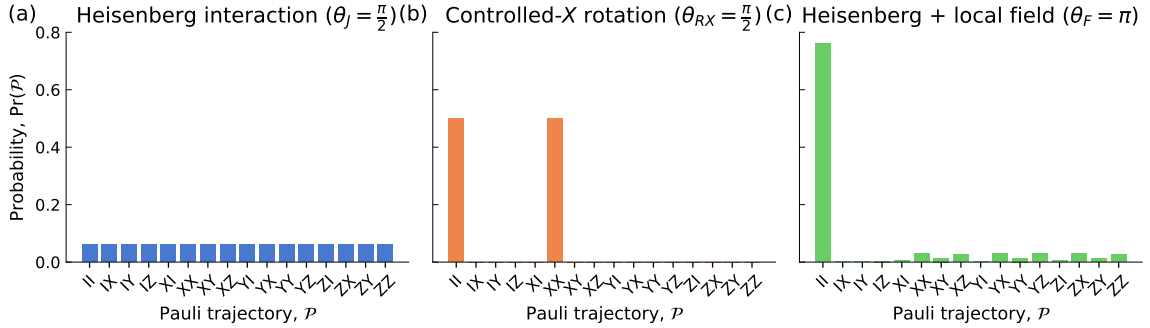


Figure 6: Example single-slot SPP trajectory distributions. (a) Heisenberg exchange interaction for $\theta_J = \pi/2$, (b) controlled- X rotation for $\theta_{RX} = \pi/2$, (c) Heisenberg exchange with local field for $\theta_F = \pi$.

For the H_{RX} model in Fig. 5(b), the GQMI is non-zero for both the original and twirled processes, indicating the presence of temporal correlations in the induced SPP. In particular, at $\theta_{RX} = \pi/2$, we find $\mathcal{I}[\Upsilon_{0:1}] = \mathcal{I}[\Upsilon_{0:1}^{\mathcal{T}_P}] = \ln 2$ and $\mathcal{J}[\Upsilon_{0:1}] = 0$, showing that the original process is Pauli-twirl invariant and hence already an SPP. This is reflected in the trajectory distribution in Fig. 6(b), where only the $I_{t_0}I_{t_1}$ and $X_{t_0}X_{t_1}$ sequences occur with non-zero probability, corresponding to a perfectly two-time correlated bit-flip channel. Away from these special points at $\theta_{RX} \neq n\pi/2$, we observe that the twirling generally reduces the GQMI while $\mathcal{J}[\Upsilon_{0:1}]$ increases, consistent with the removal of non-Pauli structure and non-Pauli-based temporal correlations.

Finally, for the local field model in Fig. 5(c), we observe a non-trivial interplay between the exchange interaction and the symmetry-breaking local field. The GQMI $\mathcal{I}[\Upsilon_{0:1}]$ is maximal at $\theta_F = 0$ (pure Heisenberg dynamics) and then decays non-monotonically as the field strength increases. In contrast to the Heisenberg-only case, the twirled GQMI $\mathcal{I}[\Upsilon_{0:1}^{\mathcal{T}_P}]$ is generically non-zero and displays oscillatory peaks and troughs as a function of θ_F . The twirl relative entropy $\mathcal{J}[\Upsilon_{0:1}]$ exhibits two distinct types of troughs which alternate with peaks in $\mathcal{I}[\Upsilon_{0:1}^{\mathcal{T}_P}]$. The trajectory probabilities in Fig. 6(c) are dominated by the $I_{t_0}I_{t_1}$ sequence, with small but correlated contributions from the Pauli sequences excluding an identity. Overall, this model highlights that SPPs can exhibit rich and structured temporal correlations, even when genuinely quantum temporal correlations are discarded.

Having established the SPP framework and illustrated it with worked examples, we now

analyse temporal correlations in one-dimensional SPP MPS representations, developing a transfer operator framework to characterise memory and correlation decay.

5 Characterising temporal correlations in 1D SPPs

Modelling SPPs within the tensor network formalism enables the application of established analytical and numerical tools to characterise the structure of spatiotemporal correlations. In this section, we primarily analyse the temporal correlation structure of SPPs to investigate how environmental memory is propagated and dissipated. We begin by defining multi-point correlation functions, evaluated via tensor contractions, which serve as the foundation for a transfer operator-based framework.

By examining the spectral properties of these operators—specifically the spectral gap and correlation length—we provide a compact characterisation of the asymptotic decay of temporal correlations. Finally, we establish an isomorphism between SPP MPS representations and hidden Markov models (HMMs) under specific constraints. This connection provides a latent-state interpretation of the Pauli dynamics and facilitates the use of existing HMM-based methods for sampling and inference in large-scale QEC studies under correlated noise.

5.1 Transfer operator framework

We begin by defining correlation functions for SPPs to quantify the statistical dependencies between Pauli operators across space and time. Since SPPs directly encode the joint probability distribution, these correlations can be straightforwardly evaluated via tensor contractions, which later motivates transfer operator formalism.

Let $f : \mathbb{P}^{(n)} \rightarrow \mathbb{R}$ be a scalar function on the set of n -qubit Pauli operators $\mathbb{P}^{(n)}$; for example, $f_X(x) = 1$ if $x = X$ and 0 otherwise. These functions play a role analogous to observables in quantum theory. Given a random Pauli operator $x_t \in \mathbb{P}^{(n)}$ at time t , the quantity $f(x_t)$ defines a real-valued random variable. For two such variables $f(x_t)$ and $g(x_{t+\tau})$ evaluated at times t and $t + \tau$, where $\tau \geq 1$, the two-point correlation function (covariance) is defined as

$$\begin{aligned} C_{f,g}(\tau) &= \mathbb{E}[(f(x_t) - \mathbb{E}[f(x_t)])(g(x_{t+\tau}) - \mathbb{E}[g(x_{t+\tau})])] \\ &= \mathbb{E}[f(x_t)g(x_{t+\tau})] - \mathbb{E}[f(x_t)]\mathbb{E}[g(x_{t+\tau})], \end{aligned} \quad (53)$$

where the expectation $\mathbb{E}[\cdot]$ is taken with respect to a full joint probability distribution $\Pr(x_0, \dots, x_k)$. At this stage, no assumptions are made regarding properties of the process such as time-homogeneity or stationarity.

In tensor network notation, each function $f(x_t)$ and $g(x_{t+\tau})$ corresponds to a real vector \mathbf{f}^{x_t} and $\mathbf{g}^{x_{t+\tau}}$ indexed by Pauli labels. The expectation values can then be computed via the full tensor contraction of these vectors with the joint probability tensor $\mathbf{p}_{x_0 \dots x_k}$ (or its MPS representation) and summing over all remaining open indices. Concretely, for single and two-point expectations, we have

$$\begin{aligned} \mathbb{E}[f(x_t)] &= \sum_{x_0, \dots, x_k} \mathbf{p}_{x_0 \dots x_k} \mathbf{f}^{x_t}, \\ \mathbb{E}[f(x_t)g(x_{t+\tau})] &= \sum_{x_0, \dots, x_k} \mathbf{p}_{x_0 \dots x_k} \mathbf{f}^{x_t} \mathbf{g}^{x_{t+\tau}}, \end{aligned} \quad (54)$$

respectively.

This construction extends directly to multi-point expectations by inserting the appropriate function vectors. To analyse these correlations more systematically, we now introduce a transfer operator-based framework.

Consider the MPS representation of an SPP with local tensors $\mathbf{A}^{\mu_t}_{x_t\mu_{t+1}}$ where $x_t \in \mathbb{P}^{(n)}$. In standard notation, this is equivalently the set of $D \times D$ matrices A_{x_t} (where $D = \dim \mu$ is the bond dimension) indexed by the x_t , with elements given by

$$(A_{x_t})_{\mu_t\mu_{t+1}} = \mathbf{A}^{\mu_t}_{x_t\mu_{t+1}}. \quad (55)$$

Given a scalar function $f : \mathbb{P}^{(n)} \rightarrow \mathbb{R}$, we define the following operators.

Definition 5.1 (Transfer and emission operators). The transfer operator T and the emission operator E_f are defined as

$$T = \sum_{x_t \in \mathbb{P}^{(n)}} A_{x_t}, \quad E_f = \sum_{x_t \in \mathbb{P}^{(n)}} f(x_t) A_{x_t}. \quad (56)$$

The transfer operator T governs how correlations propagate along the virtual (environment) bonds. The observable-inserted transfer operator E_f , which we refer to as the emission operator, encodes how an observable f couples to these bonds. A tensor graphical representation of these operators is shown in Fig. 7.

We note that the definition of the transfer operator here differs from the conventional quantum MPS transfer operator, which involves both the tensor and its complex conjugate [67]. The distinction arises because the SPP MPS directly encodes the joint probability distribution over Pauli labels, rather than quantum amplitudes.

We now assume the SPP is *time-homogeneous* (all tensors A_{x_t} are identical for all t) and *ergodic*, such that the process reaches a unique stationary state on the environment space. As a result, the transfer operator T has a unique leading eigenvalue $\lambda_1 = 1$ (after normalisation), with corresponding left and right eigenvectors $\langle l_1 |$ and $|r_1\rangle$ satisfying

$$\langle l_1 | T = \langle l_1 |, \quad T |r_1\rangle = |r_1\rangle, \quad (57)$$

with normalisation $\langle l_1 |r_1\rangle = 1$. Eigenvectors $\langle l_1 |$ and $|r_1\rangle$ thus correspond to the left and right fixed points of the transfer operator. For such stationary processes, the expectation values can be written compactly as

$$\begin{aligned} \mathbb{E}[f(x_t)] &= \langle l_1 | E_f |r_1\rangle =: \langle f \rangle, \\ \mathbb{E}[f(x_t)g(x_{t+\tau})] &= \langle l_1 | E_f T^{\tau-1} E_g |r_1\rangle =: \langle fg \rangle. \end{aligned} \quad (58)$$

To recast the covariance in terms of operators, we introduce the centred emission operator.

Definition 5.2 (Centered emission operator). The centred emission operator \tilde{E}_f corresponding to the function f is defined as

$$\tilde{E}_f = E_f - \langle f \rangle T, \quad (59)$$

satisfying $\langle l_1 | \tilde{E}_f |r_1\rangle = 0$.

This operator represents the deviation of the observable f around its stationary mean. Using this, the two-point covariance takes a canonical form,

$$C_{f,g}(\tau) = \langle l_1 | \tilde{E}_f T^{\tau-1} \tilde{E}_g |r_1\rangle. \quad (60)$$

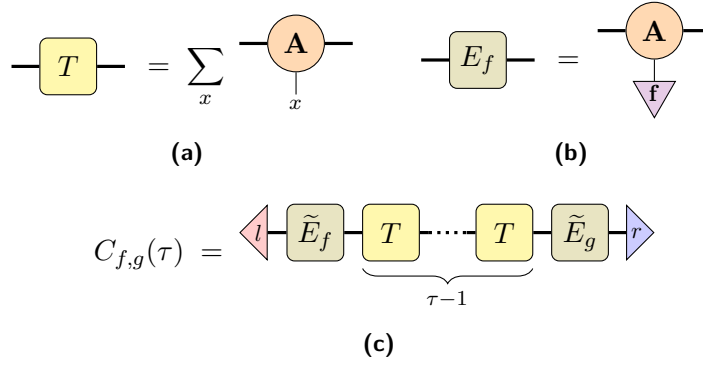


Figure 7: Transfer operator construction for 1D SPPs. Assumes a time-homogeneous SPP MPS. (a) The transfer operator $T = \sum_{x \in \mathcal{P}^{(n)}} A_x$, obtained by summing the local MPS tensors over the Pauli label x . (b) The emission (observable-inserted) operator $E_f = \sum_x f(x) A_x$, corresponding to insertion of a scalar function $f : \mathcal{P}^{(n)} \rightarrow \mathbb{R}$. (c) Two-point covariance as a function of separation τ , expressed as $C_{f,g}(\tau) = \langle l_1 | \tilde{E}_f T^{\tau-1} \tilde{E}_g | r_1 \rangle$, where $|r_1\rangle$ and $\langle l_1|$ are the right and left fixed points of T and $\tilde{E}_f = E_f - \langle l_1 | E_f | r_1 \rangle T$ is the centred emission operator.

The covariance is thus described entirely in terms of the transfer and emission operators. It follows that the decay of temporal correlations is governed by the exponent of the transfer operator T , and hence by its eigenvalue spectrum. Finally, this formulation extends naturally to multi-point correlation functions. For an ordered time sequence $t_1 < t_2 < \dots < t_m$, the m -point correlator is

$$C_{f_1, \dots, f_m} = \langle l_1 | \tilde{E}_{f_1} T^{\Delta t_1} \tilde{E}_{f_2} T^{\Delta t_2} \dots T^{\Delta t_{m-1}} \tilde{E}_{f_m} | r_1 \rangle, \quad (61)$$

where $\Delta t_j = t_{j+1} - t_j - 1$ is the number of intermediate time steps between t_j and t_{j+1} . We now turn to the spectral properties of the transfer operator to characterise the decay of these correlations over time.

5.2 Spectral gap and correlation decay

For clarity, we begin by assuming that the transfer operator T is diagonalisable. Its spectral decomposition is given by

$$T = \sum_{i=1}^D \lambda_i |r_i\rangle \langle l_i|, \quad (62)$$

where the eigenvalues are ordered by their magnitudes $|\lambda_1| \geq |\lambda_2| \geq \dots \geq |\lambda_D|$, the left and right eigenvectors satisfy $\langle l_i | r_j \rangle = \delta_{ij}$, and the leading eigenvalue is normalised as $\lambda_1 = 1$. Inserting this into the covariance function from Eq. (60) yields

$$C_{f,g}(\tau) = \sum_{i=2}^D \lambda_i^{\tau-1} \langle l | \tilde{E}_f | r_i \rangle \langle l_i | \tilde{E}_g | r \rangle. \quad (63)$$

Only the terms $i \geq 2$ contribute since the leading eigenvectors correspond to the stationary state, for which $\langle l_1 | \tilde{E}_f | r_1 \rangle = \langle l_1 | \tilde{E}_g | r_1 \rangle = 0$. This expression explicitly shows that the decay of correlations is a sum of exponentially decaying modes.

The asymptotic, long-time behaviour is dominated by the subleading eigenvalue with the second-largest magnitude, which we denote as $\lambda_* = |\lambda_2|$. From this, we define two key quantities:

1. **The spectral gap** (Δ): Defined as

$$\Delta = 1 - \lambda_*, \quad (64)$$

the spectral gap quantifies the rate of convergence to the stationary state. A large gap ($\lambda_* \ll 1$) implies correlations decay rapidly, indicating a short memory time. Conversely, a small gap ($\lambda_* \approx 1$) signifies long-lived temporal correlations.

2. **The correlation length** (ξ): The characteristic timescale of the decay is given by the correlation length,

$$\xi = -\frac{1}{\ln \lambda_*}. \quad (65)$$

In particular, for sufficiently large τ , the asymptotic decay is governed by this timescale, with $|C_{f,g}(\tau)| \sim e^{-\tau/\xi}$.

More broadly, the eigenspectrum of T provides a compact characterisation of how environmental memory is propagated and dissipated. These spectral properties remain a useful descriptor even when relaxing assumptions such as diagonalisability and ergodicity. For instance, complex eigenvalues indicate oscillatory correlation behaviour, while degenerate leading eigenvalues imply non-ergodic dynamics with multiple stationary states.

Finally, while $T = \sum_x A_x$ is generally non-Hermitian (and may be non-normal), transfer operators induced by Haar-random system-environment unitaries are diagonalisable with probability one. More generally, when T is non-normal, eigenvalues alone need not fully characterise finite-time dynamics, and transient effects may arise; in such cases pseudo-spectral methods and related non-normal spectral theory may be employed [68]. Next, we discuss how this framework extends to higher-dimensional SPPs.

5.3 Higher-dimensional generalisation

We briefly indicate how the transfer operator framework extends to higher-dimensional SPP tensor networks. In the one-dimensional case, all spatial structure is compressed into a single index, resulting in a matrix transfer operator. For higher dimensional SPPs, the transfer operator itself may be represented by a tensor network.

Concretely, consider the 2D SPP PEPS illustrated in Fig. 4, whose local tensors are given by

$$\mathbf{a}_{(i,j)}^{\nu_j^{i-1} \mu_j^i} x_j^i \mu_{j+1}^i \nu_j^i, \quad (66)$$

where i and j label spatial and temporal positions, respectively. We define the *single-site transfer tensor* $\mathbf{r}_{(i,j)}$ by summing over the local Pauli index x_j^i . That is, for each site (i, j) , we obtain

$$\mathbf{r}_{(i,j)}^{\nu_j^{i-1} \mu_j^i} \mu_{j+1}^i \nu_j^i = \sum_{x_j^i \in \mathbb{P}} \mathbf{a}_{(i,j)}^{\nu_j^{i-1} \mu_j^i} x_j^i \mu_{j+1}^i \nu_j^i. \quad (67)$$

The *row transfer operator* $\mathbf{R}_{(j)}$ is then the contraction of these tensors along the spatial bonds ν across a single row (time slice) j . Writing $\vec{\mu}_j := (\mu_j^0, \dots, \mu_j^{n-1})$ for the collection of temporal bonds (and similarly $\vec{\mu}_{j+1}$), we have

$$\mathbf{R}_{(j)}^{\vec{\mu}_j} \vec{\mu}_{j+1} = \sum_{\nu_j^0, \dots, \nu_j^{n-1}} \mathbf{r}_{(0,j)}^{\mu_j^0} \mu_{j+1}^0 \nu_j^0 \mathbf{r}_{(1,j)}^{\nu_j^0 \mu_j^1} \mu_{j+1}^1 \nu_j^1 \cdots \mathbf{r}_{(n-1,j)}^{\nu_j^{n-2} \mu_j^{n-1}} \mu_{j+1}^{n-1} \nu_j^{n-1}, \quad (68)$$

which is precisely an MPO along space.

At a high level, the previous analyses of [Sections 5.1](#) and [5.2](#) may be generalised to higher-dimensional SPPs by replacing the matrix transfer operator T with an appropriate tensor network transfer object, such as the MPO $\mathbf{R}_{(j)}$ for 2D SPP PEPS. In this setting, expectation values and correlation functions can be expressed as contractions of boundary states—typically represented by an MPS—with products of transfer and emission MPOs, in direct analogy with [Eqs. \(58\)](#) and [\(60\)](#). In the time-homogeneous case $\mathbf{R}_{(j)} \equiv \mathbf{R}$, the role of stationary vectors $\langle l_1 |$ and $|r_1\rangle$ is played by boundary MPSs, corresponding to boundary fixed points. Computation of these boundary MPSs as well as the spectral properties of the transfer MPO may require more involved numerical tensor network-based techniques [\[69, 70, 71, 62\]](#). We do not pursue these generalisations in this work, leaving them for future exploration. For the remainder of the section, we return to the one-dimensional setting and formally link MPS transfer operator description to hidden Markov model realisations.

5.4 Equivalence to hidden Markov models

An SPP MPS, together with its associated transfer operator, naturally admits a hidden state interpretation. In this view, the virtual bond indices serve as latent variables whose dynamics drive the observed Pauli sequence. We make this connection explicit by linking SPP MPS representations to finite-state classical *hidden Markov models* (HMMs). Concretely, under appropriate positivity and normalisation constraints, an SPP MPS of bond dimension D is isomorphic to an *edge-emitting* HMM with D hidden states. This equivalence provides a bridge to the extensive HMM literature, enabling efficient hidden state-based methods for sampling and modelling SPPs—tools we exploit in [Sections 6](#) and [7](#).

Let $(S_t)_{t \geq 0}$ be a Markov chain on a finite state space $\mathcal{S} = \{1, \dots, D\}$, and let $(X_t)_{t \geq 0}$ be a sequence of observations from the Pauli alphabet $\mathbb{P}^{(n)}$. An edge-emitting HMM is fully specified by an initial distribution π_i over the hidden states and a set of transition-emission kernels $(K_x)_{ij}$. The initial distribution satisfies

$$\pi_i := \Pr(S_0 = i), \quad \pi_i \geq 0, \quad \sum_{i \in \mathcal{S}} \pi_i = 1. \quad (69)$$

The transition-emission kernels $(K_x)_{ij}$ describe the joint probability of transitioning from hidden state i to $j \in \mathcal{S}$ while emitting observation $x \in \mathbb{P}^{(n)}$, defined as

$$(K_x)_{ij} := \Pr(S_{t+1} = j, X_t = x | S_t = i), \quad (70)$$

whose elements are non-negative and appropriately normalised as

$$(K_x)_{ij} \geq 0 \quad \forall i, j, x, \quad \sum_{x, j} (K_x)_{ij} = 1 \quad \forall i. \quad (71)$$

Summing over emitted symbols yields the hidden state *transition matrix*,

$$(T_{\text{HMM}})_{ij} = \sum_x (K_x)_{ij}. \quad (72)$$

By [Eq. \(71\)](#), T_{HMM} is *row-stochastic*, satisfying $\sum_j (T_{\text{HMM}})_{ij} = 1$ for all i , and hence $T_{\text{HMM}} |\mathbf{1}\rangle = |\mathbf{1}\rangle$. If the chain is ergodic, it admits a unique stationary distribution π satisfying $\pi^T T_{\text{HMM}} = \pi^T$ and $\pi^T \mathbf{1} = 1$. Accordingly, for a row-stochastic T_{HMM} , we may take $\langle l_1 | = \pi^T$ and $|r_1\rangle = |\mathbf{1}\rangle$.

The probability of observing a Pauli sequence $x_{0:k}$ is given by a marginalisation over all possible hidden state sequences,

$$\Pr(x_{0:k}) = \sum_{s_0, \dots, s_{k+1}} \pi_{s_0} \prod_{t=0}^k (K_{x_t})_{s_t s_{t+1}}. \quad (73)$$

This expression is in direct analogy with the SPP MPS probabilities in Eq. (44). We now propose sufficient conditions under which an SPP MPS is equivalent to such an HMM.

Proposition 5.3 (Sufficient conditions for SPP MPS-HMM equivalence). Let a time-homogeneous SPP be specified by an MPS $\{A_x\}_{x \in \mathbb{P}^{(n)}}$ of bond dimension D . If there exists a representation (gauge) in which A_x satisfies

$$(A_x)_{ij} \geq 0 \quad \forall i, j, x, \quad \sum_{x \in \mathbb{P}^{(n)}} \sum_{j=1}^D (A_x)_{ij} = 1 \quad \forall i, \quad (74)$$

then the process admits an edge-emitting Hidden Markov model (HMM) realisation with D hidden states under the identification

$$(K_x)_{ij} \equiv (A_x)_{ij}. \quad (75)$$

In particular, the SPP transfer matrix $T = \sum_x A_x$ coincides with the HMM transition matrix $T_{\text{HMM}} = \sum_x K_x$.

These conditions are sufficient but not necessary; a generic SPP MPS need not admit a nonnegative, row-stochastic representation of the same bond dimension. However, any non-Markovian process can be rendered Markovian by enlarging the (in general, potentially unbounded) state space [19]. Constructing such an embedding optimally is model dependent and generally nontrivial [72]. Since we are primarily interested in utilising HMMs as practical generative models for correlated noise, we do not pursue minimal HMM realisations here.

A practical advantage of HMM realisations is access to standard, efficient procedures for inference, learning, and sampling [73]. Importantly, HMMs enable simple sequential sampling of Pauli trajectories via transition-emission update rules, making them well suited to large-scale Monte Carlo studies of QEC under correlated noise. This capability underpins the numerical analyses in subsequent sections, which we turn to next.

6 Surface code performance under temporal correlations

In this section we present the first concrete application of the SPP framework, focusing on a simple, tunable model of temporally correlated Pauli noise and its consequences for surface code performance. We first position SPPs as practical QEC noise models and clarify how they may interface with standard circuit-level analyses. We then introduce the temporal storm model—a two-state SPP/HMM whose correlation length ξ (equivalently spectral gap Δ) can be swept while keeping single round marginal error rates fixed. Finally, we describe the simulation methodology and report memory and stability benchmarks, illustrating that temporal correlation structure can substantially modify logical scaling even when the average noise strength is controlled.

6.1 SPPs as effective circuit-level noise models

Up to this point, we have developed a general framework for spatiotemporal Pauli processes (SPPs). In principle, an SPP description of circuit noise can be obtained from a tomographically reconstructed process tensor [27, 25]. In practice, it is more useful to characterise an SPP directly at a chosen level of granularity—either at the circuit level, or phenomenologically at the level of QEC cycles. For the remainder of the paper, we focus on SPPs as generative noise models for QEC; broader uses, including decoding and noise mitigation, are discussed in Section 8.

Correlations in realistic device noise can substantially alter QEC performance relative to memoryless baselines. Our goal here is to not catalogue and deconstruct existing models, but to emphasise that a practical QEC-facing description of noise should (i) capture correlations at a level relevant to syndrome processing and decoding, while (ii) remain compatible with general underlying (Markovian or non-Markovian) dynamics. SPPs provide a convenient language for this purpose. Under randomised compiling, the multi-time Pauli twirl maps noisy stabiliser circuit dynamics to an effective SPP—a joint distribution over Pauli fault across space and time. This twirl is an operational construction: It does not assert that the microscopic dynamics are literally transformed into an SPP, but instead yields an effective model that captures the noise statistics relevant to stabiliser QEC (e.g., syndrome distributions and logical error rates) under the assumed randomisation protocol.

Although the SPP framework resolves correlation at the level of individual operations, large-scale simulations and decoder interfaces often motivate a coarser representation. Accordingly, in our numerical studies we adopt a hybrid description: we treat within-round circuit noise using a standard independent gate-level model, while modelling inter-round memory effects by an SPP defined at the QEC cycle level. This choice reflects three pragmatic considerations. First, Pauli noise on a Clifford syndrome extraction circuit can be coarse-grained to an effective correlated Pauli error model on data and ancilla qubits at the end or start of each cycle [74]. Second, the correlations that most strongly impact long-time performance are frequently those that manifest across multiple rounds. Third, decoders and many characterisation protocols naturally consume coarse-grained syndrome data, making a cycle-level SPP a convenient interface between microscopic noise and practical QEC tools.

In this section and the next, we exploit this bridge from microscopic dynamics, through SPPs, to efficiently simulable HMMs in two concrete settings. In Section 6, we introduce a simple one-dimensional SPP with tunable spectral gap (equivalently, tunable correlation length) while keeping marginal error rates fixed, enabling a controlled study of how temporal correlations can impact surface code memory and stability experiments. In Section 7, we turn to a genuinely spatiotemporal two-dimensional SPP derived from a quantum cellular automaton model of environmental dynamics, which generates rich correlation structure and statistical-mechanical behaviour while remaining parametrically simple. Near a critical point, the autocorrelations can exhibit multi-scale or non-single-exponential decay. The robust feature in Fig. 11(c) is therefore the existence and location of a narrow region of dramatically enhanced temporal correlations.

6.2 Temporal storm noise model

We now instantiate the general SPP formalism in a one-dimensional, analytically tunable setting, which we refer to as the *temporal storm model*. Each system qubit is coupled to its own two-level environment with classical basis states $\{|0\rangle, |1\rangle\}$, representing *calm* and *storm* conditions, respectively.

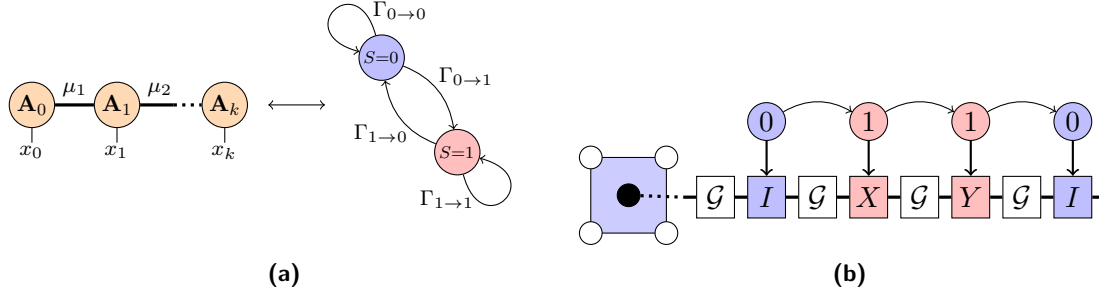


Figure 8: Temporal storm model: two-state latent memory with Pauli emissions. A two-state latent environment $s_t \in \{0, 1\}$ (calm, storm) evolves as a Markov chain and modulates the Pauli label $x_t \in \{I, X, Y, Z\}$ emitted at each time step, yielding temporally correlated Pauli noise with fixed single-round marginals. (a) Equivalent representations of the same one-dimensional SPP as an MPS and as a two-state HMM with emission probabilities $q_{s_t}^{(x)}$. (b) Cycle-level noise schematic used for our QEC simulations. Each qubit (data and ancilla) couples to an independent two-state environment; \mathcal{G} denotes a chosen granularity of circuit operations (from a single gate to an entire syndrome extraction subcircuit).

The environment undergoes a time-homogeneous classical Markov chain with transition probabilities $\Gamma_{s \rightarrow s'}$ between calm and storm (Fig. 8). The system-environment interaction is modelled as a quantum channel conditioned on the environment state. When the environment E is in state $|s'\rangle$, the system S evolves according to

$$\mathcal{E}_{s'}[\rho_S] = \sum_x q_{s'}^{(x)} \sigma^{(x)} \rho_S \sigma^{(x)}, \quad (76)$$

where $\sigma^{(x)}$ denotes the Pauli operators indexed by x , and $q_{s'}^{(x)}$ are probabilities satisfying $\sum_x q_{s'}^{(x)} = 1$. The joint system-environment evolution over a single time step is thus described by the CPTP map

$$\Phi[\rho_{SE}] = \sum_{s, s', x} K_{s's}^{(x)} \rho_{SE} K_{s's}^{(x)\dagger}, \quad K_{s's}^{(x)} = \sqrt{\Gamma_{s \rightarrow s'} q_{s'}^{(x)}} |s'\rangle\langle s|_E \otimes \sigma_S^{(x)}. \quad (77)$$

Because the environment dynamics are classical and the conditional system channels $\mathcal{E}_{s'}$ are Pauli, the corresponding process tensor is invariant under the multi-time Pauli twirl in Eq. (32). In other words, this construction directly specifies an SPP, and may be viewed as the twirled image of a family of compatible underlying process tensors.

Labelling the environment transition probabilities as $a = \Gamma_{0 \rightarrow 1}$ and $b = \Gamma_{1 \rightarrow 0}$, the corresponding transfer operator T and SPP matrices $A^{(x)}$ are

$$T = \begin{pmatrix} 1-a & a \\ b & 1-b \end{pmatrix}, \quad A^{(x)} = T \text{diag}(q_0^{(x)}, q_1^{(x)}). \quad (78)$$

This is precisely a two-state HMM where T describes the evolution of the latent state, and the Pauli emission label x_t is drawn from $q_{s_t}^{(x)}$. The spectrum of T is given by $\lambda_1 = 1, \lambda_2 = 1 - a - b$. The subleading eigenvalue λ_2 sets the spectral gap Δ and correlation length ξ ,

$$\Delta = a + b, \quad \xi = -\frac{1}{\ln(1 - a - b)}, \quad (79)$$

where we assume $0 \leq a, b \leq 1$ with $a + b < 1$, so that $\lambda_2 \in (0, 1)$ and $\xi > 0$.

The left and right eigenvectors associated with λ_1 , corresponding to the left and right stationary states, are

$$\langle l| = (\pi_0 \ \pi_1), \quad |r\rangle = \begin{pmatrix} 1 \\ 1 \end{pmatrix}, \quad (80)$$

where $\pi_0 = b/(a+b)$ and $\pi_1 = a/(a+b)$ are the stationary calm and storm fractions, respectively, and we have dropped the subscript 1 in l_1, r_1 . These immediately lead to the marginal Pauli error rates,

$$\bar{p}^{(x)} = \pi_0 q_0^{(x)} + \pi_1 q_1^{(x)} = \frac{bq_0^{(x)} + aq_1^{(x)}}{a+b}. \quad (81)$$

By solving [Eqs. \(79\)](#) and [\(81\)](#) for the transition rates a and b , we construct a family of temporally correlated noise models with tunable spectral gap Δ (or correlation length ξ) while maintaining fixed marginal error rates $\bar{p}^{(x)}$. This decoupling of environmental memory from average noise strength underpins the parameter sweeps in the surface code simulations that follow.

6.3 Simulation methodology

We benchmark surface code performance under the temporal storm noise model using two standard protocols: a memory experiment, which tests preservation of a logical observable through time, and a stability experiment, which tests the reliability of moving a logical observable through space [\[75\]](#). Memory and stability experiments may be viewed as complementary space-time duals, and together they benchmark distinct but equally vital primitives of surface code logical computation. This symmetry is particularly relevant for correlated noise. In memory experiments, correlated data qubit faults can form spacelike chains implementing a logical operator, whereas in stability experiments, temporally correlated stabiliser measurement (or ancilla-induced) faults can form timelike chains spanning many rounds, likewise inducing a logical operator.

For the memory experiment, we simulate rotated surface code circuits of distance d for $N_r = 3d$ rounds of syndrome extraction, and measure logical failure probability p_{shot} after decoding using minimum-weight perfect matching. We estimate an effective per round error rate from the per shot failure probability as $p_{\text{round}} = (1 - (1 - 2p_{\text{shot}})^{1/N_r})/2$. For the stability experiment, we simulate a diameter-4 surface code patch with a variable number of rounds N_r (setting the timelike distance), and report the logical failure probability per shot. In the parameter sweeps we use $d = 5, 7, \dots, 19$ for memory, and $N_r = 5, 10, \dots, 35$ for stability.

Noise is implemented in a hybrid manner following the modelling choice of [Section 6.2](#). We apply a global independent, gate-level baseline noise model consisting of: a single qubit depolarising channel after every single qubit Clifford gate and on each data qubit at the start of each round, a two qubit depolarising channel after each two qubit entangling gate, a Pauli X flip (Z flip) channel before Z -basis (X -basis) measurements, and after Z -basis (X -basis) state preparations. All baseline noise processes are parameterised by a single characteristic error rate $p = 0.1\%$.

Inter-round temporal correlations are incorporated by composing, at the start of each round, an additional Pauli fault on every data and ancilla qubit sampled from the temporal storm SPP described above. The circuit granularity \mathcal{G} in [Fig. 8](#) is therefore taken to be an entire syndrome extraction subcircuit per round, though the construction is valid for finer granularities. Throughout the sweep we fix the marginal error rate of the correlated errors to match the characteristic rate, $\bar{p}^{(x)} = p = 0.1\%$, and vary correlation length over

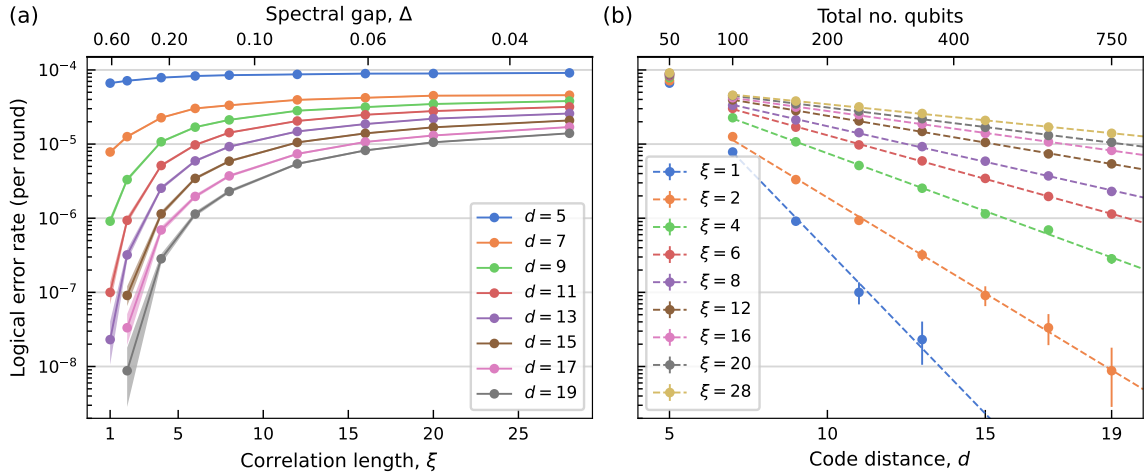


Figure 9: Surface code memory versus temporal correlation length. Fixed marginal error rate $p = 0.1\%$, variable code distance d , and $N_r = 3d$ number of rounds. (a) Effective per round logical error rate versus correlation length ξ (bottom axis), with corresponding spectral gap shown on the top axis. The per round error rate p_{round} is inferred from the per shot failure rate p_{shot} via $p_{\text{round}} = (1 - (1 - 2p_{\text{shot}})^{1/N_r})/2$. (b) The same data plotted versus code distance d at fixed ξ (legend), illustrating the degradation of distance scaling as temporal correlations increase. Dashed lines are exponential fits (excluding $d = 5$). Error bars, where visible, indicate binomial standard errors.

$\xi \in [1, 28]$. The initial state of the environment is sampled from the stationary distribution in Eq. (80).

Simulations are performed using Stim [12] for stabiliser circuit sampling, with temporally correlated errors generated externally from the temporal storm HMM. Decoding is performed using minimum-weight perfect matching via PyMatching [14] on a detector error model constructed from the independent circuit-level noise with marginal error rates matched to the correlated process. For each parameter point we estimate failure probabilities from Monte Carlo sampling over 10^7 shots; error bars, where visible, denote binomial standard errors.

6.4 Surface code memory and stability benchmarks

Figures 9 and 10 summarise surface code performance under the temporal storm model as correlation length ξ is increased at fixed marginal error rates $\bar{p}^{(x)}$. Across both benchmarks, increasing ξ systematically degrades logical performance, highlighting that correlation structure in physical noise alone can substantially alter logical behaviour.

We first consider the memory experiment. Figure 9(a) displays the per round logical error rate p_{round} as a function of ξ for several code distances. For each d , p_{round} increases monotonically with ξ , with the most pronounced shift occurring as the model crosses from nearly memoryless dynamics ($\xi = 1$) into moderate-to-long memory ($1 < \xi \leq 5$). For larger ξ , the curves tend to level off, consistent with a “bursty” noise picture in which memory concentrates faults into rarer but more damaging multi-round clusters. The $d = 5$ data trends systematically above the higher distance curves and are therefore omitted from the fit in panel (b). At the baseline error rate of $p = 0.1\%$, the distance five code provides comparatively weak error suppression even in the low memory regime, so increasing ξ degrades performance without exhibiting the same clean scaling observed at larger distances.

Figure 9(b) presents the same data as a performance-versus-distance scaling plot at fixed ξ . The logical error rate remains approximately exponentially suppressed with in-

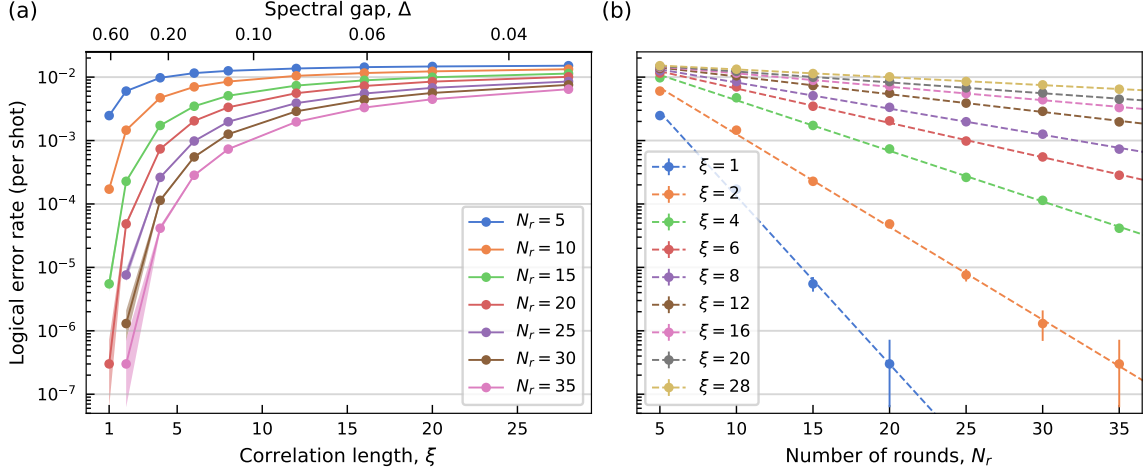


Figure 10: Surface code stability versus temporal correlation length. We fix the marginal error rate $p = 0.1\%$ for a diameter-4 surface code patch with variable number of rounds N_r . (a) Logical failure rate per shot versus correlation length ξ (bottom axis), with the corresponding spectral gap shown on the top axis. (b) The same data plotted versus number of rounds (timelike distance) N_r at fixed ξ . Dashed lines represent exponential fits, and error bars indicate binomial standard error.

creasing d , but the decay exponent decreases in magnitude markedly as ξ grows. In this sense, temporal correlations blunt, though do not eliminate, the benefit of distance scaling, consistent with an effective spacetime distance reduction. From a resource perspective, the qubit overhead required to achieve a given logical error rate is highly sensitive to growth in correlation length, for example, from $\xi = 1$ to $\xi = 2$.

We next turn to the stability experiment, which provides a complementary probe of how temporal structure affects the reliability of surface code computational primitives. Figure 10 plots the logical failure probability per shot as a function of N_r for several ξ . The same qualitative trend emerges—performance degrades markedly as ξ increases—but the stability protocol is a particularly direct diagnostic of the impact of temporal structure since logical failure is directly associated with timelike error chains. This is reflected in Fig. 10(b), where the suppression of logical failure with increasing N_r progressively weakens as ξ grows, indicating that temporal correlations erode the benefit of increasing timelike distances. The close qualitative similarity to the memory results in Fig. 9 aligns with the space-time dual interpretation of stability experiments. These results also underscore the broader importance of studying correlated noise, since correlations can non-trivially interact with primitives of logical computation even under Pauli-frame randomisation.

Throughout, decoding is performed using minimum-weight perfect matching with a detector error model constructed from the independent circuit-level noise, with marginal rates matched to the correlated process. The resulting performance degradation with increasing ξ therefore reflects, in part, decoder mismatch under standard assumptions, and motivates correlation-aware decoding or mitigation strategies leveraging the SPP framework. We discuss the matter further alongside other applications in Section 8.

7 Spatiotemporal noise via a quantum cellular automaton

While Section 6 demonstrated the impact of purely temporal correlation, noise in contemporary quantum hardware frequently exhibits genuinely spatiotemporal structure. Here we introduce a spatiotemporal SPP model derived from a two-dimensional quantum cellular

automaton (QCA) environment (bath) coupled locally to the system. Operational Pauli twirling on the system maps the underlying coherent bath dynamics to an effective SPP that admits an exact description as a probabilistic cellular automaton (PCA) with a non-linear transition kernel. We show that tuning a single parameter controlling the strength of coherent bath interactions drives the bath into a pseudo-critical regime with macroscopic error avalanches and critical slowing down, producing correlated fault patterns reminiscent of correlated error events reported in solid-state platforms. The model thus provides a microscopically motivated, yet tractably simulable, link between non-equilibrium statistical mechanics and QEC performance under spatiotemporal correlations.

We structure the analysis as follows. In [Section 7.1](#), we present the microscopic QCA model, and its mapping, under operational system twirling, to an effective SPP with an exact PCA description. In [Section 7.3](#), we characterise the resulting PCA as a statistical mechanical system, isolating how the spatial parameter controlling coherent bath interactions drives a critical-like transition in the bath dynamics. Finally, in [Section 7.4](#), we benchmark rotated surface code memory under this noise model and show a sharp breakdown of distance scaling in the pseudo-critical regime.

7.1 Microscopic QCA dynamics

We define the microscopic dynamics of the QCA noise model on a 2D square lattice V . At each site $i \in V$, a system qubit S_i is locally coupled to an environment (bath) qubit E_i . We impose a checkerboard bipartition of the lattice $V = V_{\text{red}} \cup V_{\text{black}}$, such that nearest neighbours $N(i)$ of a red site are strictly black, and vice versa. The environment is initialised as a classical mixture of Z -basis states, completely uncorrelated with the system.

The joint single-cycle CPTP map is defined as the composition of a local environment storm channel (as in [Section 6](#)), a two-layer coherent QCA update, and a system-environment interaction. Formally, we define the joint map as

$$\mathcal{M}_{a,b,\theta} := \mathcal{U}^{SE} \circ \mathcal{Q}_{B \rightarrow R}^E(\theta) \circ \mathcal{Q}_{R \rightarrow B}^E(\theta) \circ \mathcal{S}^E(a, b). \quad (82)$$

We detail the constituent maps below.

1. Environment storm channel, $\mathcal{S}^E(a, b)$

Each environment qubit undergoes an independent storm process flipping each qubit from $|0\rangle \rightarrow |1\rangle$ with probability a , and from $|1\rangle \rightarrow |0\rangle$ with probability b . The map for each site i is

$$\mathcal{S}^{(i)}(a, b)[\rho] = \sum_k L_k \rho L_k^\dagger, \quad (83)$$

with Kraus operators,

$$L_0 = \sqrt{a} |1\rangle\langle 0|, \quad L_1 = \sqrt{1-a} |0\rangle\langle 0|, \quad L_2 = \sqrt{b} |0\rangle\langle 1|, \quad L_3 = \sqrt{1-b} |1\rangle\langle 1|. \quad (84)$$

The global channel is the product over sites, $\mathcal{S}^E(a, b) = \bigotimes_{i \in V} \mathcal{S}^{(i)}(a, b)$.

2. QCA half-step (red \rightarrow black), $\mathcal{Q}_{R \rightarrow B}^E(\theta)$

The QCA update is implemented as a layer of two commuting controlled- X rotations with the red and black sublattices as alternating controls and targets. For the first half-step with red controls and black targets, we define the unitary

$$Q_{R \rightarrow B}(\theta) = \prod_{i \in V_{\text{red}}} \prod_{j \in N(i)} \left(|0\rangle\langle 0|^{E_i} \otimes I^{E_j} + |1\rangle\langle 1|^{E_i} \otimes e^{-i\theta X^{E_j}} \right). \quad (85)$$

The corresponding channel is denoted

$$\mathcal{Q}_{R \rightarrow B}^E(\theta)[\rho] = Q_{R \rightarrow B}(\theta)\rho Q_{R \rightarrow B}^\dagger(\theta). \quad (86)$$

3. QCA half-step (black \rightarrow red), $\mathcal{Q}_{B \rightarrow R}^E(\theta)$

For the second half-step with black controls and red targets, we define the unitary

$$Q_{B \rightarrow R}(\theta) = \prod_{i \in V_{\text{black}}} \prod_{j \in N(i)} \left(|0\rangle\langle 0|^{E_i} \otimes I^{E_j} + |1\rangle\langle 1|^{E_i} \otimes e^{-i\theta X^{E_j}} \right), \quad (87)$$

with corresponding channel

$$\mathcal{Q}_{B \rightarrow R}^E(\theta)[\rho] = Q_{B \rightarrow R}(\theta)\rho Q_{B \rightarrow R}^\dagger(\theta). \quad (88)$$

Together, these two maps implement a full QCA update on the environment.

4. Environment-system unitary, \mathcal{U}^{SE}

Each environment qubit E_i couples locally to the system qubit S_i via a controlled unitary interaction. We define

$$U_{SE}^{(i)} = \sum_{k=0}^1 |k\rangle\langle k|^{E_i} \otimes V_k^{S_i}, \quad U_{SE} = \bigotimes_{i \in V} U_{SE}^{(i)}, \quad \mathcal{U}^{SE}[\rho] = U_{SE}\rho U_{SE}^\dagger, \quad (89)$$

The key structural assumption is that the conditional unitaries $\{V_k\}$ are orthogonal under the Hilbert-Schmidt inner product,

$$V_k V_l^\dagger = I \forall k, \quad \text{Tr}(V_k V_l) = 0 \forall k \neq l. \quad (90)$$

Furthermore, in this work, we specialise to the minimal family of unitaries

$$V_0 = I, \quad V_1 = \vec{n} \cdot \vec{\sigma} = n_X X + n_Y Y + n_Z Z, \quad \|\vec{n}\|^2 = 1, \quad (91)$$

with $\vec{n} \in \mathbb{R}^3$.

The entire dynamics are thus governed by three parameters: two temporal parameters (a, b) specifying the environment storm channel $\mathcal{S}^E(a, b)$, and a third spatial parameter θ controlling the coherent QCA on the environment.

To obtain the effective SPP, we apply the multi-time Pauli twirl \mathcal{T}_P^S on $\mathcal{M}_{a,b,\theta}$ exclusively on the system subspace. Because the maps $\mathcal{S}^E(a, b)$ and $\mathcal{Q}_{B \rightarrow R}^E(\theta)$, $\mathcal{Q}_{R \rightarrow B}^E(\theta)$ act trivially on the system, the twirl can be ‘pushed through’ to act solely on the interaction \mathcal{U}^{SE} . Defining the twirled interaction as $\tilde{\mathcal{U}}^{SE} := \mathcal{T}_P^S[\mathcal{U}^{SE}]$, we write the effective twirled joint map

$$\tilde{\mathcal{M}}_{a,b,\theta} := \mathcal{T}_P^S[\mathcal{M}_{a,b,\theta}] = \tilde{\mathcal{U}}^{SE} \circ \mathcal{Q}_{B \rightarrow R}^E(\theta) \circ \mathcal{Q}_{R \rightarrow B}^E(\theta) \circ \mathcal{S}^E(a, b). \quad (92)$$

The central mechanism of this model is that, for a system-environment interaction of the controlled-unitary form in Eq. (89), satisfying the orthogonality condition in Eq. (90), the system twirl induces an effective Z -basis dephasing on the environment in each cycle. Explicitly, for each site i the reduced environment update obeys

$$\text{Tr}_{S_i}(\tilde{\mathcal{U}}^{SE}[\rho_{S_i E_i}]) = \sum_{k \in \{0,1\}} |k\rangle\langle k|_{E_i} \text{Tr}_{S_i}[\rho_{S_i E_i}] |k\rangle\langle k|_{E_i}, \quad (93)$$

which removes the off-diagonal components of the environment state in the computational basis. Crucially, we do not impose a dephasing channel on the bath by hand. Rather, this re-classicalisation of the environment emerges as a direct consequence of interacting with the operationally twirled system.

This construction yields three key features of the effective dynamics:

1. **Nonlinear transition kernel:** The QCA step reduces to a PCA with a nonlinear transition kernel, with the probability of a target site flipping given by $p = \sin^2(k\theta)$ as a function of the number of k excited neighbours.
2. **Environment re-classicalisation:** The twirled interaction applies an effective Z -basis dephasing to the environment every cycle, re-classicalising the bath and collapsing any coherent superpositions.
3. **System Pauli noise:** Conditioned on the environment state, the induced system noise is a Pauli channel with relative weights set by the coefficients n_X^2, n_Y^2, n_Z^2 of the conditional unitary V_1 .

Altogether, coherent local bath dynamics combined with operational system twirling produce a microscopically derived spatiotemporal noise model that is local and causal by construction, and that admits an exact description as a PCA hidden Markov model (HMM). Full derivations of the mapping and the properties above are given in [Section C](#). We now summarise the resulting PCA HMM dynamics.

7.2 Effective probabilistic cellular automaton

The effective spatiotemporal SPP admits an exact description as a classical HMM with a nonlinear transition kernel, where the nonlinearity is inherited from coherent interactions in the underlying QCA. The latent state is the environment bath configuration, and the emissions are the system Pauli faults.

Let $s_t(i) \in \{0, 1\}$ denote the state of environment site $i \in V$ at the beginning of cycle t . The Pauli emission pattern during cycle t is denoted by the string $x_t \in \{x_t(i)\}_{i \in V}$, where each $x_t(i) \in \{I, X, Y, Z\}$ is sampled conditional on the updated bath configuration $s_{t+1}(i)$ at the end of the cycle.

Crucially, because the lattice is bipartite, each PCA half-step updates only one sublattice, and the update probability at a site depends only on the (fixed) configuration of the opposite sublattice. Consequently, conditioned on the opposite sublattice, updates are independent across sites within the active sublattice. This eliminates update collisions and renders the model highly parallelisable.

0. **Environment initialisation:** Choose an initial distribution π_0 over configurations $s_0 \in \{0, 1\}^{|V|}$ and sample $s_0 \sim \pi_0$.
1. **Storm update:** Given s_t , generate the intermediate configuration $s_{t'}$ by updating each site $i \in V$ independently as
 - if $s_t(i) = 0$, set $s_{t'}(i) \leftarrow 1$ with probability a ;
 - if $s_t(i) = 1$, set $s_{t'}(i) \leftarrow 0$ with probability b ;
 - else set $s_{t'}(i) \leftarrow s_t(i)$.
2. **PCA half-step (black):** Generate the next intermediate state $s_{t''}$ by updating each black site $i \in V_{\text{black}}$, conditioned on the red configuration as
 - for each $i \in V_{\text{black}}$, compute the number of excited red neighbours $k(i) = \sum_{j \in N(i)} s_{t'}(j)$;
 - set $s_{t''}(i) \leftarrow s_{t'}(i) \oplus 1$ with probability $\sin^2(k(i)\theta)$, else set $s_{t''}(i) \leftarrow s_{t'}(i)$;
 - for each $i \in V_{\text{red}}$, set $s_{t''}(i) \leftarrow s_{t'}(i)$.

3. **PCA half-step (red)**: Complete the PCA step to generate s_{t+1} as

- for each $i \in V_{\text{red}}$, compute the number of excited black neighbours $k(i) = \sum_{j \in N(i)} s_{t''}(j)$;
- set $s_{t+1}(i) \leftarrow s_{t''}(i) \oplus 1$ with probability $\sin^2(k(i)\theta)$, else set $s_{t+1}(i) \leftarrow s_{t''}(i)$;
- for each $i \in V_{\text{black}}$, set $s_{t+1}(i) \leftarrow s_{t''}(i)$.

4. **Pauli emission**: For each site $i \in V$, sample the system Pauli emissions x_t as

- if $s_{t+1}(i) = 0$, sample $x_t(i) = I$;
- if $s_{t+1}(i) = 1$, sample $x_t(i) \in \{X, Y, Z\}$ with probabilities n_X^2, n_Y^2, n_Z^2 , respectively.

The resulting Pauli string $x_t = \{x_t(i)\}_{i \in V}$ is the noise induced on the system during cycle t .

5. **Repeat**: Increment t , and repeat steps 1-4 for as many cycles required.

The PCA describes a driven classical spin system with a nonlinear update rule. The storm process continuously injects and removes excitations locally, while the QCA-derived PCA spread excitations across the lattice in a neighbour-dependent manner parametrised by θ . Importantly, the nonlinear transition kernel $p = \sin^2(k\theta)$ is a uniquely quantum footprint of the coherent bath effects. The competition between these stochastic perturbations and nonlinear spatial propagations gives rise to non-trivial steady states and spatiotemporal correlation structures, which we evaluate next.

7.3 Criticality and spatiotemporal correlations

Before studying the noise properties of this model for QEC, we first analyse the PCA dynamics from [Section 7.2](#) as a statistical mechanical system. In particular, we isolate the effect of the spatial parameter θ , which controls the strength of the nonlinear PCA update via kernel $p = \sin^2(k\theta)$, on the emergent correlation structure and steady-state properties of the system.

Throughout, we fix the storm parameters to a low spontaneous injection rate $a = 10^{-4}$ and a fast local relaxation rate $b = 0.5$, and sweep the controlled-rotation angle $\theta \in [0, \pi]$. Pauli emission weights are taken to be uniform (unbiased) with $n_X = n_Y = n_Z = 1/\sqrt{3}$. We consider lattices corresponding to rotated surface code layouts for distances $d = 9, 11, 13, 15$, with the number of sites (qubits) $N_d = |V| = 2d^2 - 1$. To quantify the excitation statistics in the environment, we define the global density at time step t as

$$\eta_t := \frac{1}{N_d} \sum_{i \in V} s_t(i), \quad (94)$$

and compute the statistics of the time series $\{\eta_t\}$. We simulate the bath dynamics up to $t = 10^6$ cycles, recording statistics only after a burn-in period of 2×10^5 cycles. This procedure is repeated for 10 independent trajectories.

[Figure 11](#) summarises three complementary diagnostics as a function of θ : the mean density $\langle \eta \rangle$, the scaled variance $N_d \text{Var}(\eta)$, and a fitted correlation time ξ_η extracted from the autocorrelations of η_t .

[Figure 11\(a\)](#) shows the mean density $\langle \eta \rangle = \langle \eta_t \rangle_t$. For small θ , the PCA step is weak, and the dynamics are dominated by the storm process. Due to the strong relaxation

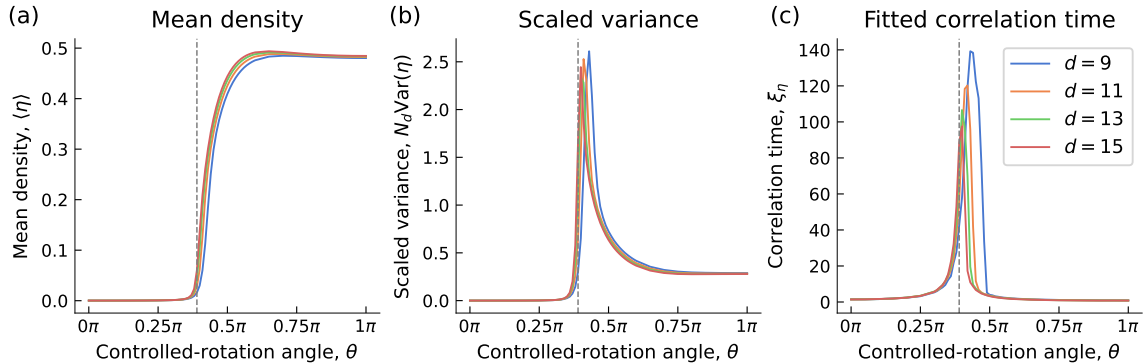


Figure 11: Pseudo-criticality and critical slowing down in the QCA-induced PCA. We fix the storm parameters to $a = 10^{-4}$ and $b = 0.5$, and sweep the spatial coupling parameter θ , which controls the strength of coherent bath interactions. Data are shown for lattice corresponding to rotated surface code patches of distances $d = 9, 11, 13, 15$ (number of sites $N_d = 2d^2 - 1$). As a function of θ , we plot (a) the mean activity (spin) density $\langle \eta_t \rangle_t$, where $\eta_t := N_d^{-1} \sum_{i \in V} s_t(i)$; (b) the scaled variance $N_d \text{Var}(\eta_t)$; and (c) the correlation time ξ_η extracted by fitting the normalised autocorrelation $C(\tau) \propto e^{-\tau/\xi_\eta}$. The vertical dashed line marks the estimated pseudo-critical threshold $\theta_{\text{th}} \approx 0.39\pi$.

$b = 0.5$, the bath remains in an effectively inactive or calm phase with a low background density $\langle \eta \rangle \approx 2 \times 10^{-4}$. As θ increases, the density undergoes a sharp, continuous crossover beginning around $\theta \approx 0.35\pi$. The neighbour-dependent spreading outpaces the local decay, driving the bath into an active steady state that saturates near $\langle \eta \rangle \approx 0.5$.

To probe the density fluctuations, we compute the scaled variance $N_d \text{Var}(\eta)$, with $\text{Var}(\eta) = \langle \eta_t^2 \rangle - \langle \eta_t \rangle^2$, reported in Fig. 11(b). This quantity is analogous to susceptibility in equilibrium statistical mechanics. We observe a pronounced, narrow peak at $\theta \approx 0.4\pi$, aligned with the sharp rise in mean density. This indicates a massive enhancement of macroscopic fluctuations, where in this near-critical regime, small local clusters of errors can spontaneously grow into system-wide avalanches before dying out. Over the evaluated system sizes, the peak exhibits a slight sharpening and shifting characteristic of finite-size scaling near a critical point.

Finally, to quantify memory in the bath dynamics, we compute the normalised autocorrelation function of the density time series,

$$C(\tau) = \frac{\langle (\eta_t - \langle \eta \rangle)(\eta_{t+\tau} - \langle \eta \rangle) \rangle_t}{\text{Var}(\eta)}, \quad (95)$$

and fit it to an exponential decay $C(\tau) \propto e^{-\tau/\xi_\eta}$ to extract the effective correlation time. As shown in Fig. 11(c), ξ_η spikes dramatically near the transition threshold, reaching $\xi_\eta \approx 140$ cycles for $d = 9$, consistent with a critical slowing down. Deep in either the calm or fully active phases, the bath relaxes rapidly ($\xi_\eta \lesssim 3$), corresponding to nearly Markovian dynamics. However, in the crossover regime, the competition between coherent spreading and stochastic decay leads to the emergence of macroscopic temporal memory.

In summary, tuning a single spatial parameter θ drives the environment through a critical-like transition from a calm, weakly correlated background into a dense, active phase. The intermediate critical window maximises both density fluctuations and temporal memory. We demonstrate below that this regime is highly detrimental for QEC, where enhanced susceptibility drives spatially correlated error avalanches, while critical slowing down causes these cascades to persist across multiple QEC cycles. We next evaluate surface code performance under these dynamics reusing the same model parameters.

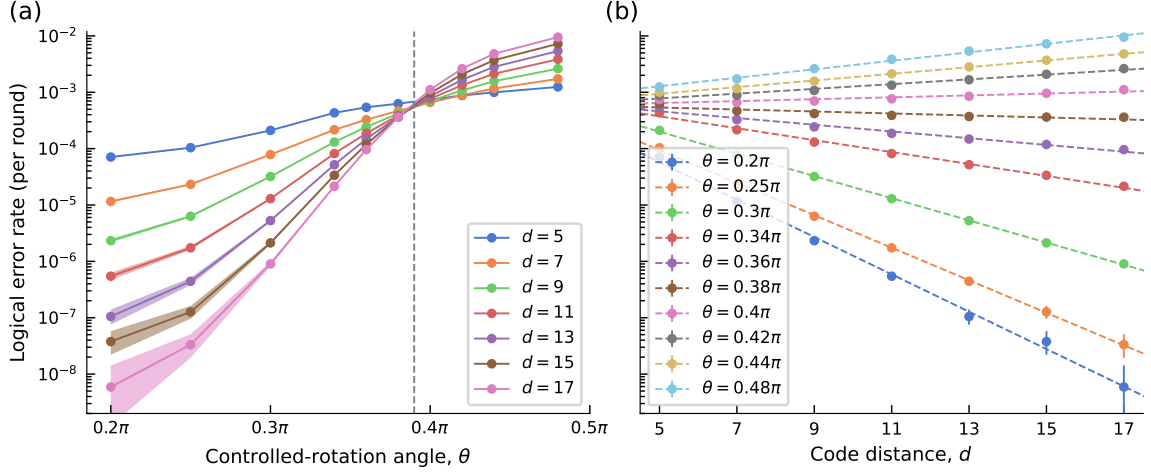


Figure 12: Surface code breakdown near pseudo-critical spatiotemporal noise. We fix $a = 10^{-4}$ and $b = 0.5$, and sweep the spatial coupling parameter θ controlling the strength of coherent bath interactions at a baseline circuit-level noise rate of 0.1%. Distances d are simulated for $N_r = 3d$ rounds. (a) Effective per-round logical error rate versus θ for various d ; the vertical dashed line marks the pseudo-critical threshold $\theta_{\text{th}} \approx 0.39\pi$. (b) The same data versus distance d at fixed θ ; dashed lines are exponential fits. Error bars, where visible, indicate binomial standard errors.

7.4 Surface code breakdown near pseudo-criticality

We now evaluate surface code memory performance under the QCA noise model. As in Section 7.3, we fix the storm parameters to $a = 10^{-4}$ and $b = 0.5$, and sweep the controlled-rotation angle θ .

The simulation protocol mirrors the surface code memory benchmark of Section 6. We simulate rotated surface code circuits of distance d for $N_r = 3d$ rounds of syndrome extraction, applying the same global circuit-level baseline noise model at a characteristic rate 0.1%. Logical failure rates are estimated via Monte Carlo sampling using Stim and decoding with minimum-weight perfect matching (MWPM) via PyMatching.

Inter-round correlated faults are incorporated by composing, at the start of each round, an additional Pauli fault sampled from the QCA-derived SPP, driven by the bath dynamics parameters (a, b, θ) . A key distinction from the temporal storm sweep is that the spatially interacting PCA bath does not admit a simple closed-form expression for marginal Pauli error rates. Accordingly, we numerically estimate the required marginal error rate for each θ to construct a marginalised detector error model for the MWPM decoder. Additionally, the bath is initialised in the all-zeros configuration for each shot.

Figure 12 details the logical error rate per round. In the calm regime ($\theta \lesssim 0.34\pi$), logical performance improves rapidly with increasing code distance. This behaviour is consistent with dilute bath excitations and weak spatiotemporal structure, where the surface code remains effective at error suppression as previously explored [60]. As θ enters the pseudo-critical window ($\theta \approx 0.36\pi$ – 0.40π), logical performance degrades sharply, and increasing code distance no longer yields reliable exponential suppression. Above a threshold $\theta_{\text{th}} \approx 0.39\pi$, the distance scaling trend entirely reverses where larger codes perform worse than smaller ones. The scaling plot in Fig. 12(b) makes this breakdown explicit.

These trends align directly with the statistical mechanical diagnostics from Section 7.3. The same θ window that strongly degrades QEC performance coincides with the regime that maximises density fluctuations and exhibits critical slowing down. In this regime, enhanced susceptibility corresponds to rare but large spatiotemporal ‘avalanches’—

spacetime-cone-like error clusters that can grow into system-side cascades before dying out. Qualitatively similar error burst mechanisms have been reported in recent experiments on superconducting qubits, for example due to cosmic rays [4, 76, 7] or leakage events [3, 77].

Taken together, these results establish a concrete mechanism by which coherence in local microscopic bath dynamics can manifest, after operational twirling, as tunable non-equilibrium criticality that substantially impacts QEC performance.

Finally, we emphasise that MWPM with a marginalised detector model does not exploit correlations. Correlation-aware decoders, or approaches utilising reweighting and model learning, may partially recover performance, but typically incur significant complexity overheads. In this sense, the QCA model offers an efficiently simulable stress test. It is derived from microscopic dynamics, exhibits nontrivial spatiotemporal correlations, and induces a breakdown of standard QEC protocols.

We now conclude by discussing future directions and extensions unlocked by the SPP framework.

8 Discussion

In this work, we introduced *spatiotemporal Pauli processes* (SPPs) to bridge the gap between the microscopic, non-Markovian descriptions of device dynamics and the stochastic Pauli noise models that form the backbone of stabiliser-based QEC theory. By applying the multi-time Pauli twirl to general process tensors, we established a framework that retains essential spatiotemporal correlations while naturally interfacing with the discrete Pauli-fault description required for scalable QEC simulation and decoding.

Our approach systematically addressed this challenge through both formal construction and numerical benchmarking. In Section 4, we formalised SPPs as the multi-time Pauli-twirled image of a general process tensor, demonstrating that this projection yields a rigorous joint distribution over spatiotemporal Pauli trajectories. Through Sections 3 and 4, we showed that these processes admit constructive tensor network representations whose internal bond dimensions are physically bounded by the environment’s Liouville dimension. To interpret these structures, Section 5 developed a transfer operator formalism, connected operator spectra to correlation length scales, and established a link to hidden Markov model representations. Finally, in Sections 6 and 7, we deployed this framework to benchmark primitives of surface code computation under controlled temporal correlations and genuinely spatiotemporal quantum cellular automaton dynamics. Notably, we demonstrated how tuning coherent bath interactions drives the system into a pseudo-critical regime, causing a sharp breakdown of surface code distance scaling.

Looking forward, the SPP framework opens several concrete avenues for the characterisation and mitigation of correlated noise in near-term and fault-tolerant architectures. Because an SPP is a bona fide stochastic process, it supports a suite of interpretable diagnostics—such as transfer operator spectra, correlation times, and heavy-tail indicators—that can be computed directly from the model. This establishes a concrete path towards *SPP learning*, fitting an efficient SPP parameterisation (e.g., a low-bond-dimension tensor network or finite-state HMM) to experimental time-series data. Such models could be learned directly from coarse-grained syndrome streams [56, 57] for *in situ* monitoring, or via extending Pauli-noise learning protocols [78, 79, 1, 80] to the multi-time case borrowing ideas from process tensor tomography [28, 25].

Once learned, these models enable a range of targeted QEC applications. Chief among these is correlation-aware decoding. Standard algorithms like minimum-weight perfect matching can be augmented with SPP-derived priors [81] (e.g., dynamic edge weights),

while more general decoders, such as belief propagation [82] or machine learning approaches [83, 84, 85] can exploit temporal correlation to improve performance. Beyond decoding and mitigation, SPPs provide generative test-beds for optimising QEC protocols themselves, for instance, by tailoring quantum error correcting codes [61] or syndrome extraction circuits to a device’s spatiotemporal correlation structure [86].

Ultimately, the success of large-scale fault-tolerant quantum computing hinges on our ability to model and correct the noise that physically occurs in hardware. By providing a rigorous, operational translation from general non-Markovian open quantum dynamics to structured, classically simulable distributions over spatiotemporal Pauli faults, SPPs narrow the gap between microscopic physical reality and practical quantum error correction. In doing so, they furnish a new toolkit for modelling correlation structure and diagnosing correlated failure modes, supporting correlation-aware decoding, mitigation, and protocol optimisation in regimes relevant to near-term and future quantum devices.

Acknowledgments

This research was supported by the Commonwealth through an Australian Government Research Training Program Scholarship [DOI: <https://doi.org/10.82133/C42F-K220>]. This research is supported by the Ministry of Education, Singapore, under its Academic Research Fund (AcRF) Tier 1 grant, and funded through the SUTD Kickstarter Initiative (SKI 2021_07_02). John F Kam is supported by a CSIRO Future Science Platform Scholarship and the Agency for Science, Technology and Research (A*STAR) Research Attachment Programme (ARAP) at the Quantum Innovation Centre (Q.InC).

Data and code availability

The datasets and code used in this study are publicly available at <https://github.com/jkfids/corrqec2>.

References

- [1] Robin Harper and Steven T. Flammia. ‘Learning Correlated Noise in a 39-Qubit Quantum Processor’. In: *PRX Quantum* 4.4 (17th Oct. 2023), p. 040311.
- [2] John F Kam et al. ‘Detrimental Non-Markovian Errors for Surface Code Memory’. In: *Quantum Science and Technology* 10.3 (16th July 2025), p. 035060.
- [3] M. McEwen et al. ‘Removing Leakage-Induced Correlated Errors in Superconducting Quantum Error Correction’. In: *Nature Communications* 12.1 (19th Mar. 2021), p. 1761.
- [4] Matt McEwen et al. ‘Resolving Catastrophic Error Bursts from Cosmic Rays in Large Arrays of Superconducting Qubits’. In: *Nature Physics* 18.1 (1st Jan. 2022), pp. 107–111.
- [5] Rajeev Acharya et al. ‘Quantum Error Correction below the Surface Code Threshold’. In: *Nature* 638.8052 (1st Feb. 2025), pp. 920–926.
- [6] G. Bratrud et al. ‘Measurement of Correlated Charge Noise in Superconducting Qubits at an Underground Facility’. In: *Nature Communications* 16.1 (11th Nov. 2025), p. 9906.

- [7] Patrick M. Harrington et al. ‘Synchronous Detection of Cosmic Rays and Correlated Errors in Superconducting Qubit Arrays’. In: *Nature Communications* 16.1 (11th July 2025), p. 6428.
- [8] B. D. Clader et al. ‘Impact of Correlations and Heavy Tails on Quantum Error Correction’. In: *Physical Review A* 103.5 (24th May 2021), p. 052428.
- [9] Dorit Aharonov, Alexei Kitaev and John Preskill. ‘Fault-Tolerant Quantum Computation with Long-Range Correlated Noise’. In: *Physical Review Letters* 96.5 (7th Feb. 2006), p. 050504.
- [10] Barbara M. Terhal and Guido Burkard. ‘Fault-Tolerant Quantum Computation for Local Non-Markovian Noise’. In: *Physical Review A* 71.1 (31st Jan. 2005), p. 012336.
- [11] Hui Khoon Ng and John Preskill. ‘Fault-Tolerant Quantum Computation versus Gaussian Noise’. In: *Physical Review A* 79.3 (16th Mar. 2009), p. 032318.
- [12] Craig Gidney. ‘Stim: A Fast Stabilizer Circuit Simulator’. In: *Quantum* 5 (July 2021), p. 497.
- [13] Oscar Higgott. ‘PyMatching: A Python Package for Decoding Quantum Codes with Minimum-Weight Perfect Matching’. In: *ACM Transactions on Quantum Computing* 3.3 (30th June 2022), 16:1–16:16.
- [14] Oscar Higgott and Craig Gidney. ‘Sparse Blossom: Correcting a Million Errors per Core Second with Minimum-Weight Matching’. In: *Quantum* 9 (Jan. 2025), p. 1600.
- [15] Eric Dennis et al. ‘Topological Quantum Memory’. In: *Journal of Mathematical Physics* 43.9 (20th Aug. 2002), pp. 4452–4505.
- [16] Austin G. Fowler et al. ‘Surface Codes: Towards Practical Large-Scale Quantum Computation’. In: *Physical Review A* 86.3 (18th Sept. 2012), p. 032324.
- [17] Heinz-Peter Breuer and Francesco Petruccione. *The Theory of Open Quantum Systems*. Oxford University Press, 25th Jan. 2007.
- [18] Heinz-Peter Breuer et al. ‘Colloquium: Non-Markovian Dynamics in Open Quantum Systems’. In: *Reviews of Modern Physics* 88.2 (19th Apr. 2016), p. 021002.
- [19] Simon Milz and Kavan Modi. ‘Quantum Stochastic Processes and Quantum Non-Markovian Phenomena’. In: *PRX Quantum* 2.3 (14th July 2021), p. 030201.
- [20] Felix A. Pollock et al. ‘Non-Markovian Quantum Processes: Complete Framework and Efficient Characterization’. In: *Physical Review A* 97.1 (25th Jan. 2018), p. 012127.
- [21] G. Chiribella, G. M. D’Ariano and P. Perinotti. ‘Quantum Circuit Architecture’. In: *Physical Review Letters* 101.6 (4th Aug. 2008), p. 060401.
- [22] Giulio Chiribella, Giacomo Mauro D’Ariano and Paolo Perinotti. ‘Theoretical Framework for Quantum Networks’. In: *Physical Review A* 80.2 (31st Aug. 2009), p. 022339.
- [23] Ognjan Oreshkov, Fabio Costa and Časlav Brukner. ‘Quantum Correlations with No Causal Order’. In: *Nature Communications* 3.1 (2nd Oct. 2012), p. 1092.
- [24] Fabio Costa and Sally Shrapnel. ‘Quantum Causal Modelling’. In: *New Journal of Physics* 18.6 (24th June 2016), p. 063032.
- [25] G. A. L. White et al. ‘Unifying Non-Markovian Characterization with an Efficient and Self-Consistent Framework’. In: *Physical Review X* 15.2 (9th May 2025), p. 021047.
- [26] Philip Taranto et al. *Higher-Order Quantum Operations*. 12th Mar. 2025. Pre-published.

- [27] G. A. L. White et al. ‘Demonstration of Non-Markovian Process Characterisation and Control on a Quantum Processor’. In: *Nature Communications* 11.1 (9th Dec. 2020), p. 6301.
- [28] G.A.L. White et al. ‘Non-Markovian Quantum Process Tomography’. In: *PRX Quantum* 3.2 (27th May 2022), p. 020344.
- [29] Gregory A. L. White. *Many-Time Physics in Practice: Characterising and Controlling Non-Markovian Quantum Stochastic Processes*. 8th May 2024. Pre-published.
- [30] Xinfang Zhang et al. ‘Learning and Forecasting Open Quantum Dynamics with Correlated Noise’. In: *Communications Physics* 8.1 (18th Jan. 2025), p. 29.
- [31] Fumiyoshi Kobayashi et al. *Tensor-Network Decoders for Process Tensor Descriptions of Non-Markovian Noise*. 18th Dec. 2024. Pre-published.
- [32] Daniel Gottesman. *Stabilizer Codes and Quantum Error Correction*. 28th May 1997. Pre-published.
- [33] M. Silva et al. ‘Scalable Protocol for Identification of Correctable Codes’. In: *Physical Review A* 78.1 (24th July 2008), p. 012347.
- [34] Easwar Magesan et al. ‘Modeling Quantum Noise for Efficient Testing of Fault-Tolerant Circuits’. In: *Physical Review A* 87.1 (22nd Jan. 2013), p. 012324.
- [35] Joel J. Wallman and Joseph Emerson. ‘Noise Tailoring for Scalable Quantum Computation via Randomized Compiling’. In: *Physical Review A* 94.5 (18th Nov. 2016), p. 052325.
- [36] Matthew Ware et al. ‘Experimental Pauli-frame Randomization on a Superconducting Qubit’. In: *Physical Review A* 103.4 (8th Apr. 2021), p. 042604.
- [37] Stefanie J. Beale and Joel J. Wallman. *Randomized Compiling in Fault-Tolerant Quantum Computation*. 23rd June 2023. Pre-published.
- [38] Aditya Jain et al. ‘Improved Quantum Error Correction with Randomized Compiling’. In: *Physical Review Research* 5.3 (25th July 2023), p. 033049.
- [39] Christopher J. Wood, Jacob D. Biamonte and David G. Cory. ‘Tensor Networks and Graphical Calculus for Open Quantum Systems’. In: *Quantum Information and Computation* 15.9–10 (2015), pp. 0759–0811.
- [40] B. Schumacher and R. F. Werner. *Reversible Quantum Cellular Automata*. 28th May 2004. Pre-published.
- [41] Terry Farrelly. ‘A Review of Quantum Cellular Automata’. In: *Quantum* 4 (Nov. 2020), p. 368.
- [42] Zhenhuan Liu, Yunlong Xiao and Zhenyu Cai. *Non-Markovian Noise Suppression Simplified through Channel Representation*. 15th Dec. 2024. Pre-published.
- [43] Hongfeng Liu et al. *Realizing Universal Non-Markovian Noise Suppression*. 25th Nov. 2025. Pre-published.
- [44] Joris Kattemölle, Balázs Gulácsi and Guido Burkard. *Non-Markovianity Induced by Pauli-twirling*. 9th Feb. 2026. Pre-published.
- [45] Alireza Seif, Moein Malekakhlagh and Swarnadeep Majumder Luke C. G. Govia. *Single Snapshot Non-Markovianity of Pauli Channels*. 13th Feb. 2026. Pre-published.
- [46] Michael A. Nielsen and Isaac L. Chuang. *Quantum Computation and Quantum Information: 10th Anniversary Edition*. Cambridge: Cambridge University Press, 2010.

- [47] Emanuel Knill and Raymond Laflamme. ‘Theory of Quantum Error-Correcting Codes’. In: *Physical Review A* 55.2 (1st Feb. 1997), pp. 900–911.
- [48] Daniel Gottesman. *The Heisenberg Representation of Quantum Computers*. 1st July 1998. Pre-published.
- [49] Scott Aaronson and Daniel Gottesman. ‘Improved Simulation of Stabilizer Circuits’. In: *Physical Review A* 70.5 (30th Nov. 2004), p. 052328.
- [50] Daniel Greenbaum and Zachary Dutton. ‘Modeling Coherent Errors in Quantum Error Correction’. In: *Quantum Science and Technology* 3.1 (20th Dec. 2017), p. 015007.
- [51] Eric Huang, Andrew C. Doherty and Steven Flammia. ‘Performance of Quantum Error Correction with Coherent Errors’. In: *Physical Review A* 99.2 (12th Feb. 2019), p. 022313.
- [52] Andrew S. Darmawan and David Poulin. ‘Tensor-Network Simulations of the Surface Code under Realistic Noise’. In: *Physical Review Letters* 119.4 (July 2017), p. 040502.
- [53] Mark Myers et al. *Simulating General Noise Nearly as Cheaply as Pauli Noise*. 8th Dec. 2025. Pre-published.
- [54] Stefanie J. Beale et al. ‘Quantum Error Correction Decoheres Noise’. In: *Physical Review Letters* 121.19 (5th Nov. 2018), p. 190501.
- [55] Joseph K Iverson and John Preskill. ‘Coherence in Logical Quantum Channels’. In: *New Journal of Physics* 22.7 (31st July 2020), p. 073066.
- [56] Thomas Wagner et al. ‘Optimal Noise Estimation from Syndrome Statistics of Quantum Codes’. In: *Physical Review Research* 3.1 (31st Mar. 2021), p. 013292.
- [57] Thomas Wagner et al. ‘Pauli Channels Can Be Estimated from Syndrome Measurements in Quantum Error Correction’. In: *Quantum* 6 (Sept. 2022), p. 809.
- [58] Ants Remm et al. *Experimentally Informed Decoding of Stabilizer Codes Based on Syndrome Correlations*. 24th Feb. 2025. Pre-published.
- [59] Jonathan Kunjummen and Jacob M. Taylor. *In Situ Calibration of Unitary Operations during Quantum Error Correction*. 2nd Nov. 2025. Pre-published.
- [60] Austin G. Fowler and John M. Martinis. ‘Quantifying the Effects of Local Many-Qubit Errors and Nonlocal Two-Qubit Errors on the Surface Code’. In: *Physical Review A* 89.3 (12th Mar. 2014), p. 032316.
- [61] Andrew Tanggara, Mile Gu and Kishor Bharti. *Strategic Code: A Unified Spatio-Temporal Framework for Quantum Error-Correction*. 27th May 2024. Pre-published.
- [62] Jonathan Keeling et al. *Process Tensor Approaches to Non-Markovian Quantum Dynamics*. 9th Sept. 2025. Pre-published.
- [63] Moritz Cygorek and Erik M. Gauger. ‘Understanding and Utilizing the Inner Bonds of Process Tensors’. In: *SciPost Physics* 18.1 (20th Jan. 2025), p. 024.
- [64] Neil Dowling et al. ‘Capturing Long-Range Memory Structures with Tree-Geometry Process Tensors’. In: *Physical Review X* 14.4 (21st Oct. 2024), p. 041018.
- [65] Mathias R. Jørgensen and Felix A. Pollock. ‘Exploiting the Causal Tensor Network Structure of Quantum Processes to Efficiently Simulate Non-Markovian Path Integrals’. In: *Physical Review Letters* 123.24 (9th Dec. 2019), p. 240602.
- [66] P Figueroa-Romero et al. ‘Operational Markovianization in Randomized Benchmarking’. In: *Quantum Science and Technology* 9.3 (30th Apr. 2024), p. 035020.

- [67] U. Schollwöck. ‘The Density-Matrix Renormalization Group’. In: *Reviews of Modern Physics* 77.1 (26th Apr. 2005), pp. 259–315.
- [68] Lloyd N. Trefethen and Mark Embree. *Spectra and Pseudospectra: The Behavior of Nonnormal Matrices and Operators*. Princeton, NJ: Princeton University Press, 2005. 606 pp.
- [69] Román Orús. ‘A Practical Introduction to Tensor Networks: Matrix Product States and Projected Entangled Pair States’. In: *Annals of Physics* 349 (1st Oct. 2014), pp. 117–158.
- [70] Sergey Bravyi, Martin Suchara and Alexander Vargo. ‘Efficient Algorithms for Maximum Likelihood Decoding in the Surface Code’. In: *Physical Review A* 90.3 (25th Sept. 2014), p. 032326.
- [71] A. Strathearn et al. ‘Efficient Non-Markovian Quantum Dynamics Using Time-Evolving Matrix Product Operators’. In: *Nature Communications* 9.1 (20th Aug. 2018), p. 3322.
- [72] M. Vidyasagar. ‘The Complete Realization Problem for Hidden Markov Models: A Survey and Some New Results’. In: *Mathematics of Control, Signals, and Systems* 23.1 (1st Dec. 2011), pp. 1–65.
- [73] Leonard E. Baum et al. ‘A Maximization Technique Occurring in the Statistical Analysis of Probabilistic Functions of Markov Chains’. In: *The Annals of Mathematical Statistics* 41.1 (1st Feb. 1970), pp. 164–171.
- [74] Spiro Gicev, Lloyd C. L. Hollenberg and Muhammad Usman. ‘Quantum Computer Error Structure Probed by Quantum Error Correction Syndrome Measurements’. In: *Physical Review Research* 6.4 (9th Dec. 2024), p. 043249.
- [75] Craig Gidney. ‘Stability Experiments: The Overlooked Dual of Memory Experiments’. In: *Quantum* 6 (24th Aug. 2022), p. 786.
- [76] Xuegang Li et al. ‘Cosmic-Ray-Induced Correlated Errors in Superconducting Qubit Array’. In: *Nature Communications* 16.1 (20th May 2025), p. 4677.
- [77] Tan He et al. ‘Experimental Quantum Error Correction below the Surface Code Threshold via All-Microwave Leakage Suppression’. In: *Physical Review Letters* 135.26 (22nd Dec. 2025), p. 260601.
- [78] Alexander Erhard et al. ‘Characterizing Large-Scale Quantum Computers via Cycle Benchmarking’. In: *Nature Communications* 10.1 (25th Nov. 2019), p. 5347.
- [79] Steven T Flammia and Joel J Wallman. ‘Efficient Estimation of Pauli Channels’. In: *ACM Transactions on Quantum Computing* 1.1 (2020), pp. 1–32.
- [80] Evan T. Hockings, Andrew C. Doherty and Robin Harper. ‘Scalable Noise Characterization of Syndrome-Extraction Circuits with Averaged Circuit Eigenvalue Sampling’. In: *PRX Quantum* 6.1 (25th Feb. 2025), p. 010334.
- [81] Volodymyr Sivak, Michael Newman and Paul Klimov. ‘Optimization of Decoder Priors for Accurate Quantum Error Correction’. In: *Physical Review Letters* 133.15 (11th Oct. 2024), p. 150603.
- [82] Pavel Panteleev and Gleb Kalachev. ‘Degenerate Quantum LDPC Codes With Good Finite Length Performance’. In: *Quantum* 5 (Nov. 2021), p. 585.
- [83] Spiro Gicev, Lloyd C. L. Hollenberg and Muhammad Usman. ‘A Scalable and Fast Artificial Neural Network Syndrome Decoder for Surface Codes’. In: *Quantum* 7 (July 2023), p. 1058.

- [84] Johannes Bausch et al. ‘Learning High-Accuracy Error Decoding for Quantum Processors’. In: *Nature* 635.8040 (1st Nov. 2024), pp. 834–840.
- [85] Spiro Gicev, Lloyd C. L. Hollenberg and Muhammad Usman. *Fully Convolutional 3D Neural Network Decoders for Surface Codes with Syndrome Circuit Noise*. 19th June 2025. Pre-published.
- [86] Matt McEwen, Dave Bacon and Craig Gidney. ‘Relaxing Hardware Requirements for Surface Code Circuits Using Time-dynamics’. In: *Quantum* 7 (7th Nov. 2023), p. 1172.

A Notation translation table

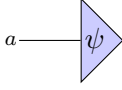
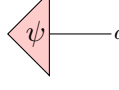
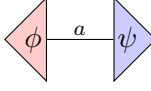
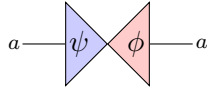
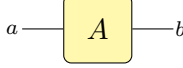
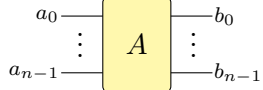
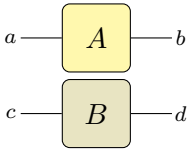
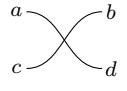
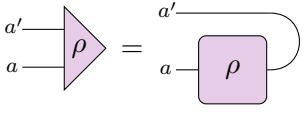
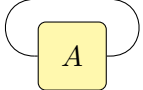
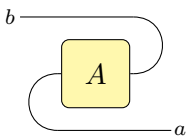
Dirac notation	Abstract index notation	Graphical calculus
State vector (ket) $ \psi\rangle$	ψ^a	
Dual vector (bra) $\langle\psi $	ψ_a	
Inner product $\langle\phi \psi\rangle$	$\phi_a\psi^a$	
Outer product $ \psi\rangle\langle\phi $	$\psi^a\phi_a$	
Operator A	A^a_b	
Multipartite operator A	$A^{a_0\dots a_{n-1}}_{b_0\dots b_{n-1}}$	
Tensor product $A \otimes B$	$A^a_b B^c_d$	
Identity \mathbb{I}	δ^a_b	
SWAP	$\delta^a_d\delta^c_b$	
Unnormalised Bell state $ \Phi^+\rangle = \mathbb{I}\rangle\rangle$	δ^{ab}	
Vectorised operator $ \rho\rangle\rangle$	$\rho^{a'a} = \rho^a_i\delta^{a'i}$	
Trace $\text{Tr}(A)$	A^i_i	
Transpose $A \rightarrow A^T$	$A^a_b \rightarrow A^b_a$	

Table 1: Translation table of common quantum objects. Equivalent notation of quantum objects and operations in Dirac notation, abstract index notation, and graphical (tensor network) calculus.

B Proof of process-separability of SPPs

Here, we provide the proof of [Theorem 4.3](#).

Proof. The dynamics of a k -slot process tensor are described by its Choi operator $\Upsilon_{0:k} \in \mathcal{B}(\mathcal{H}_{\Upsilon_{0:k}})$, where $\mathcal{H}_{\Upsilon_{0:k}} := \bigotimes_{j=0}^k (\mathcal{H}_{i_j} \otimes \mathcal{H}_{o_j})$. We expand $\Upsilon_{0:k}$ in the Pauli basis on each input-output pair as

$$\Upsilon_{0:k} = \sum_{\vec{\mu}, \vec{\nu}} \chi_{\vec{\mu}, \vec{\nu}} \bigotimes_{j=0}^k (P_{\mu_j} \otimes P_{\nu_j}), \quad (\text{B1})$$

denoting $\vec{\mu} = (\mu_0, \mu_1, \dots, \mu_k)$ and $\vec{\nu} = (\nu_0, \nu_1, \dots, \nu_k)$. Here the Pauli operators P_{μ_j} and P_{ν_j} act on \mathcal{H}_{i_j} and \mathcal{H}_{o_j} , respectively. Up to a convention-dependent normalisation factor, $\chi_{\vec{\mu}, \vec{\nu}}$ are real coefficients given by

$$\chi_{\vec{\mu}, \vec{\nu}} = \text{Tr} [P_{\vec{\mu}, \vec{\nu}} \Upsilon_{0:k}], \quad P_{\vec{\mu}, \vec{\nu}} := \bigotimes_{j=0}^k (P_{\mu_j} \otimes P_{\nu_j}). \quad (\text{B2})$$

The multi-time Pauli twirl $\mathcal{T}_P^{(k)}$ is defined in [Theorem 4.1](#), which we restate here,

$$\Upsilon_{0:k}^{\mathcal{T}_P} := \mathcal{T}_P^{(k)}(\Upsilon_{0:k}) = \frac{1}{|\mathbb{P}^{(n)}|^{k+1}} \sum_{Q_0, \dots, Q_k \in \mathbb{P}^{(n)}} \left(\bigotimes_{j=0}^k Q_j \otimes Q_j \right) \Upsilon_{0:k} \left(\bigotimes_{j=0}^k Q_j \otimes Q_j \right). \quad (\text{B3})$$

Substituting the Pauli expansion from [Eq. \(B1\)](#) yields

$$\Upsilon_{0:k}^{\mathcal{T}_P} = \frac{1}{|\mathbb{P}^{(n)}|^{k+1}} \sum_{Q_0, \dots, Q_k \in \mathbb{P}^{(n)}} \sum_{\vec{\mu}, \vec{\nu}} \chi_{\vec{\mu}, \vec{\nu}} \bigotimes_{j=0}^k (Q_j P_{\mu_j} Q_j \otimes Q_j P_{\nu_j} Q_j). \quad (\text{B4})$$

Using the Pauli conjugation averaging identity,

$$\frac{1}{|\mathbb{P}^{(n)}|} \sum_{Q \in \mathbb{P}^{(n)}} (QP_\mu Q) \otimes (QP_\nu Q) = \delta_{\mu, \nu} (P_\mu \otimes P_\nu), \quad (\text{B5})$$

all cross terms in $\chi_{\vec{\mu}, \vec{\nu}}$ with $\vec{\mu} \neq \vec{\nu}$ in [Eq. \(B4\)](#) vanish, simplifying the expression to

$$\Upsilon_{0:k}^{\mathcal{T}_P} = \sum_{\vec{\xi}} \tilde{\chi}_{\vec{\xi}} \bigotimes_{j=0}^k (P_{\xi_j} \otimes P_{\xi_j}), \quad (\text{B6})$$

where we have relabelled the remaining coefficients as $\tilde{\chi}_{\vec{\xi}} = \chi_{\vec{\xi}, \vec{\xi}}$, $\vec{\xi} = (\xi_0, \xi_1, \dots, \xi_k)$.

To prove the absence of quantum temporal correlations, we must show that $\Upsilon_{0:k}^{\mathcal{T}_P}$ is separable across the bipartitions between distinct time steps. The key insight is that the Bell basis states, $|\beta_i\rangle \in \{|\Phi^+\rangle, |\Phi^-\rangle, |\Psi^+\rangle, |\Psi^-\rangle\}$ (for a single qubit example), are simultaneous eigenvectors of operators of the form $P_\xi \otimes P_\xi$. Consequently, $\Upsilon_{0:k}^{\mathcal{T}_P}$ is diagonal in the Bell product basis $|\mathcal{B}_{\vec{\alpha}}\rangle = \bigotimes_{j=0}^k |\beta_{\alpha_j}\rangle$. Explicitly, we perform the change of basis

$$\Upsilon_{0:k}^{\mathcal{T}_P} = \sum_{\vec{\alpha}, \vec{\beta}} \lambda_{\vec{\alpha}, \vec{\beta}} |\mathcal{B}_{\vec{\alpha}}\rangle \langle \mathcal{B}_{\vec{\beta}}|, \quad \lambda_{\vec{\alpha}, \vec{\beta}} := \langle \mathcal{B}_{\vec{\alpha}} | \sum_{\vec{\xi}} \tilde{\chi}_{\vec{\xi}} \bigotimes_{j=0}^k (P_{\xi_j} \otimes P_{\xi_j}) | \mathcal{B}_{\vec{\beta}} \rangle, \quad (\text{B7})$$

and since $|\mathcal{B}_{\vec{\alpha}}\rangle$ are eigenvectors of $\bigotimes_{j=0}^k (P_{\xi_j} \otimes P_{\xi_j})$, we have $\lambda_{\vec{\alpha}, \vec{\beta}} = 0$ for all $\vec{\alpha} \neq \vec{\beta}$. Hence, we may write

$$\Upsilon_{0:k}^{\mathcal{T}_P} = \sum_{\vec{\alpha}} \lambda_{\vec{\alpha}} |\mathcal{B}_{\vec{\alpha}}\rangle \langle \mathcal{B}_{\vec{\alpha}}|, \quad \lambda_{\vec{\alpha}} := \langle \mathcal{B}_{\vec{\alpha}} | \sum_{\vec{\xi}} \tilde{\chi}_{\vec{\xi}} \bigotimes_{j=0}^k (P_{\xi_j} \otimes P_{\xi_j}) | \mathcal{B}_{\vec{\alpha}} \rangle. \quad (\text{B8})$$

Because $\Upsilon_{0:k}^{\mathcal{T}_P}$ is positive semidefinite and the vectors $|\mathcal{B}_{\vec{\alpha}}\rangle$ form an eigenbasis, the corresponding eigenvalues $\lambda_{\vec{\alpha}}$ in Eq. (B8) are non-negative. Moreover, since $\Upsilon_{0:k}^{\mathcal{T}_P}$ is diagonal in the Bell product basis, its trace is the sum of these eigenvalues,

$$\sum_{\vec{\alpha}} \lambda_{\vec{\alpha}} = \text{Tr}[\Upsilon_{0:k}^{\mathcal{T}_P}] = \text{Tr}[\Upsilon_{0:k}], \quad (\text{B9})$$

where the equality follows from the trace preservation of the twirl. Hence, $\Upsilon_{0:k}^{\mathcal{T}_P}$ is manifestly process-separable (cf. Eq. (15)), and the normalised weights $p_{\vec{\alpha}} = \lambda_{\vec{\alpha}}/\text{Tr}[\Upsilon_{0:k}]$ define a probability distribution as in Eq. (35).

Finally, the coefficients $\lambda_{\vec{\alpha}}$ can be related to the Pauli decomposition coefficients $\tilde{\chi}_{\vec{\xi}}$ via a Walsh-Hadamard transform,

$$\lambda_{\vec{\alpha}} = \sum_{\vec{\xi}} \tilde{\chi}_{\vec{\xi}} \prod_{j=0}^k M_{\alpha_j \xi_j}, \quad M_{\alpha \xi} := \langle \beta_{\alpha} | (P_{\xi} \otimes P_{\xi}) | \beta_{\alpha} \rangle. \quad (\text{B10})$$

□

C Derivation of QCA to PCA HMM mapping

In this appendix, we derive the effective PCA HMM from the microscopic QCA noise model under the system Pauli twirl. We first summarise the setting and assumptions in Section C.1, then derive the effective environment dephasing in Section C.2, the PCA kernel in Section C.3, and the system Pauli emission channel in Section C.4. Finally, we summarise the full mapping in Section C.5.

C.1 Setting and assumptions

We fix the microscopic QCA noise model from Section 7.1 and collect here the standing assumptions and notation used to derive the effective PCA HMM. The environment consists of qubits on a bipartite graph $V = R \cup B$ (red/black sublattices). Throughout, $\{|s\rangle\}$ denotes the computational basis of the environment Hilbert space, with $s \in \{0, 1\}^{|V|}$, and we write $\Pi_s := |s\rangle\langle s|$. For the bipartition we use

$$s = (r, b) \in \{0, 1\}^{|R|} \times \{0, 1\}^{|B|}, \quad |s\rangle = |r\rangle_R \otimes |b\rangle_B, \quad (\text{C1})$$

with corresponding projectors $\Pi_r^R := |r\rangle\langle r|_R$ and $\Pi_b^B := |b\rangle\langle b|_B$. For a site $j \in B$ we denote its red neighbours by $N_R(j) \subseteq R$, and similarly for $i \in R$ we denote its black neighbours by $N_B(i) \subseteq B$. We now summarise the setting and assumptions for the mapping.

- (A1) **Classical environment initialisation.** Before any dynamics, the environment is initialised as a mixture of computational basis states

$$\rho_E = \sum_s \text{Pr}(s) \Pi_s. \quad (\text{C2})$$

- (A2) **Single cycle structure.** One cycle of the microscopic dynamics is the composition of (i) an environment-only storm channel \mathcal{S}^E , (ii) two QCA half-steps $\mathcal{Q}^E = \mathcal{Q}_{B \rightarrow R}^E \circ \mathcal{Q}_{R \rightarrow B}^E$ on the environment, and (iii) a local system-environment unitary interaction \mathcal{U}^{SE} , as detailed in Section 7.

- (A3) **QCA unitaries.** Denote the QCA half-step unitaries as $Q_{R \rightarrow B}^E(\theta)$ and $Q_{B \rightarrow R}^E(\theta)$ for $Q_{R \rightarrow B}^E$ and $Q_{B \rightarrow R}^E$ respectively. Fix $\theta \in \mathbb{R}$, and for each directed edge $i \rightarrow j$ with $i \in R$, $j \in B$, define the controlled X -rotation on the target E_j ,

$$U_{i \rightarrow j}(\theta) := |0\rangle\langle 0|_{E_i} \otimes I_{E_j} + |1\rangle\langle 1|_{E_i} \otimes e^{i\theta X_{E_j}}. \quad (\text{C3})$$

The unitary $Q_{R \rightarrow B}^E(\theta)$ is the product of these (commuting) gates over all such edges,

$$Q_{R \rightarrow B}^E(\theta) := \prod_{j \in B} \prod_{i \in N_R(j)} U_{i \rightarrow j}(\theta). \quad (\text{C4})$$

Similarly, $Q_{B \rightarrow R}^E(\theta)$ is defined by swapping the roles of R and B .

- (A4) **System-environment interaction.** At each site, the system interacts locally with the corresponding environment qubit via a controlled unitary

$$U_{SE} = \sum_{z \in \{0,1\}} \Pi_z^E \otimes V_z^S, \quad (\text{C5})$$

where $\Pi_z^E := |z\rangle\langle z|_E$. In general, the conditional unitaries $\{V_z\}$ must be orthogonal under the Hilbert-Schmidt inner product,

$$\text{Tr}(V_z V_{z'}^\dagger) = d_S \delta_{z,z'}, \quad (\text{C6})$$

where d_S is the local system dimension. In this work, we specialise to

$$V_0 = I, \quad V_1 = \vec{n} \cdot \vec{\sigma} = n_X X + n_Y Y + n_Z Z, \quad \|\vec{n}\|^2 = 1, \quad (\text{C7})$$

for some $\vec{n} \in \mathbb{R}^3$.

- (A5) **System Pauli twirl.** Each cycle includes Pauli-frame randomisation on the system, yielding the effective (local) system-environment interaction

$$\tilde{U}^{SE}[\rho] = \frac{1}{4} \sum_{P \in \{I, X, Y, Z\}} (I \otimes P) U_{SE} (I \otimes P) \rho (I \otimes P) U_{SE}^\dagger (I \otimes P). \quad (\text{C8})$$

For later use, it is convenient to record the general Kraus representation for \tilde{U}^{SE} . Inserting Eq. (C5) into the above,

$$\tilde{U}^{SE}[\rho] = \sum_P \sum_{z,z'} K_{P,z} \rho K_{P,z'}^\dagger, \quad K_{P,z} = \frac{1}{2} \Pi_z \otimes (P V_z P). \quad (\text{C9})$$

We now proceed to derive the effective PCA kernel and system Pauli emission channel under these assumptions.

C.2 Environment re-classicalisation induced by system twirling

We first show that, under the system Pauli twirl, the reduced action of the system-environment interaction on the environment is exactly a Z -basis dephasing channel. This is the mechanism by which the environment is re-classicalised at each cycle.

For a single site (suppressing the site index), let ρ_S be an arbitrary (fixed) system state, and define the reduced environment channel induced by the twirled interaction \tilde{U}^{SE} in (A5) as

$$\mathcal{E}[\rho_E] = \text{Tr}_S(\tilde{U}^{SE}[\rho_E \otimes \rho_S]), \quad (\text{C10})$$

Using the Kraus representation in Eq. (C9), we may write

$$\begin{aligned}
\mathcal{E}[\rho_E] &= \sum_P \sum_{z,z'} \text{Tr}_S(K_{P,z}(\rho_E \otimes \rho_S)K_{P,z'}^\dagger) \\
&= \sum_P \sum_{z,z'} \frac{1}{4} \text{Tr}_S((\Pi_z \otimes PV_z P)(\rho_E \otimes \rho_S)(\Pi_{z'} \otimes PV_{z'} P)^\dagger) \\
&= \sum_{z,z'} \Pi_z \rho_E \Pi_{z'} \cdot \frac{1}{4} \sum_P \text{Tr}(PV_z P \rho_S P V_{z'}^\dagger P).
\end{aligned} \tag{C11}$$

By the cyclicity of the trace and $P^2 = I$, we express

$$\mathcal{E}[\rho_E] = \sum_{z,z'} \Pi_z \rho_E \Pi_{z'} \cdot \text{Tr}(V_z \frac{1}{4} \sum_P (P \rho_S P) V_{z'}^\dagger). \tag{C12}$$

The Pauli average inside the trace is the completely depolarising channel on ρ_S ,

$$\frac{1}{4} \sum_{P \in \{I, X, Y, Z\}} P \rho_S P = \frac{\mathbb{I}}{2}. \tag{C13}$$

So Eq. (C12) becomes,

$$\mathcal{E}[\rho_E] = \sum_{z,z'} \Pi_z \rho_E \Pi_{z'} \cdot \frac{1}{2} \text{Tr}(V_z V_{z'}^\dagger), \tag{C14}$$

Invoking the Hilbert-Schmidt orthogonality in Eq. (C6), we obtain

$$\mathcal{E}[\rho_E] = \sum_z \Pi_z \rho_E \Pi_z. \tag{C15}$$

That is, the reduced environment update is exactly dephasing in the computational basis, and independent of the choice of ρ_S . For the full environment lattice, the interaction $U_{SE} = \bigotimes_{i \in V} U_{SE}^{(i)}$ factorises across sites and the twirl is applied locally, so the reduced environment update also factorises as

$$\Delta_E[\rho] := \bigotimes_{i \in V} \sum_{z \in \{0,1\}} \Pi_z^{E_i} \rho \Pi_z^{E_i} = \sum_{s \in \{0,1\}^{|V|}} \Pi_s \rho \Pi_s, \tag{C16}$$

For use in the next section, we also define the sublattice dephasing channels

$$\Delta_B[\rho] := \sum_b (\Pi_b^B \otimes I_R) \rho (\Pi_b^B \otimes I_R), \quad \Delta_R[\rho] := \sum_r (I_B \otimes \Pi_r^R) \rho (I_B \otimes \Pi_r^R), \tag{C17}$$

such that $\Delta_E = \Delta_B \circ \Delta_R = \Delta_R \circ \Delta_B$.

C.3 Derivation of the PCA kernel

We now derive the effective classical update rule generated by the coherent QCA step under the per-cycle environment dephasing derived in Section C.2. Concretely, we evaluate the map $\rho_E \mapsto (\Delta_E \circ \mathcal{Q}^E)[\rho_E]$ for an initial classical state ρ_E as in (A1). We show that this is equivalent to a two-step PCA update with flip probabilities $\sin^2(k\theta)$, where k is the number of excited neighbours in the opposite sublattice. Note that although the storm channel \mathcal{S}^E precedes \mathcal{Q}^E , it does not affect the form of the PCA kernel, since it is a classical channel that preserves the diagonal structure of ρ_E .

First, we fix an environment basis configuration $s = (r, b)$ and consider the action of $Q_{R \rightarrow B}^E(\theta)$ from (A3). For a single directed edge (gate) $i \rightarrow j$ with $i \in R, j \in B$,

$$U_{i \rightarrow j}(\theta)[|r_i\rangle \otimes |\psi\rangle_j] = |r_i\rangle \otimes (e^{-i\theta X_{E_j}})^{r_i} |\psi\rangle_j. \quad (\text{C18})$$

The control bit $r_i \in \{0, 1\}$ controls whether to apply an X -rotation to the target j or to do nothing. For a fixed target $j \in B$, the product over its red neighbours yields

$$\prod_{i \in N_R(j)} U_{i \rightarrow j}(\theta)[|r\rangle \otimes |\psi\rangle_j] = |r\rangle \otimes (e^{-ik_j(r)\theta X_{E_j}}) |\psi\rangle_j, \quad (\text{C19})$$

where $k_j(r) := \sum_{i \in N_R(j)} r_i$ is the number of excited red neighbours. Because gates on distinct targets j commute, the full first half-step acts as

$$Q_{R \rightarrow B}(\theta)[|r\rangle \otimes |b\rangle] = |r\rangle \otimes \bigotimes_{j \in B} (e^{-ik_j(r)\theta X_{E_j}}) |b_j\rangle. \quad (\text{C20})$$

By the exact same reasoning, $Q_{B \rightarrow R}(\theta)$ can be written as

$$Q_{B \rightarrow R}(\theta)[|r\rangle \otimes |b\rangle] = \bigotimes_{i \in R} (e^{-ik_i(b)\theta X_{E_i}}) |r_i\rangle \otimes |b\rangle, \quad (\text{C21})$$

The key observation is that $Q_{B \rightarrow R}(\theta)$ (the *second* half-step) in Eq. (C21) uses B only as a computational-basis control. As a result, it can be written as the block-diagonal operator

$$Q_{B \rightarrow R}(\theta) = \sum_b \Pi_b^B \otimes W_b^R, \quad (\text{C22})$$

for some unitaries W_b^R on R . In this form, we can express the action of Δ_B on the second half-step as

$$\Delta_B[Q_{B \rightarrow R} \rho Q_{B \rightarrow R}^\dagger] = Q_{B \rightarrow R} \Delta_B[\rho] Q_{B \rightarrow R}^\dagger, \quad (\text{C23})$$

i.e., the commutation relation $\Delta_B \circ Q_{B \rightarrow R} = Q_{B \rightarrow R} \circ \Delta_B$.

Now using $\Delta_E = \Delta_R \circ \Delta_B$, we may write

$$\Delta_E \circ Q = \Delta_R \circ \Delta_B \circ Q_{B \rightarrow R} \circ Q_{R \rightarrow B} = \Delta_R \circ Q_{B \rightarrow R} \circ \Delta_B \circ Q_{R \rightarrow B}. \quad (\text{C24})$$

This expression allows us to insert Δ_B immediately after the first half-step $Q_{R \rightarrow B}$. Crucially, this enables us to show that the intermediate coherences in B generated by the first half-step do not affect the final distribution, and that the two QCA half-step unitaries can be treated as separate PCA updates.

We now evaluate the action of $\Delta_B \circ Q_{R \rightarrow B}$ on a basis state $|r\rangle|b\rangle$. For a single site $j \in B$ and any $\varphi \in \mathbb{R}$, recall

$$e^{-i\varphi X} |0\rangle = \cos(\varphi) |0\rangle - i \sin(\varphi) |1\rangle, \quad e^{-i\varphi X} |1\rangle = \cos(\varphi) |1\rangle - i \sin(\varphi) |0\rangle. \quad (\text{C25})$$

Hence, for $z \in \{0, 1\}$,

$$\Delta_z[e^{-i\varphi X} |z\rangle\langle z| e^{i\varphi X}] = \cos^2(\varphi) |z\rangle\langle z| + \sin^2(\varphi) |1 \oplus z\rangle\langle 1 \oplus z|, \quad (\text{C26})$$

since off-diagonal terms are removed by the dephasing.

We now take $\varphi = k_j(r)\theta$. Using the factorised form of $Q_{R \rightarrow B}$ in Eq. (C20), we can therefore interpret $\Delta_B \circ Q_{R \rightarrow B}$ as a classical flip rule on each black site $j \in B$, conditional on r . Explicitly, the bit $b_j \mapsto b'_j$ is flipped with probability

$$\Pr(b'_j = b_j \oplus 1 | r) = \sin^2(k_j(r)\theta), \quad \Pr(b'_j = b_j | r) = \cos^2(k_j(r)\theta). \quad (\text{C27})$$

Furthermore, because $\mathcal{Q}_{R \rightarrow B}$ factorises across j in Eq. (C20), the per-site updates can be applied independently across j .

By the exact same logic, the map $\Delta_R \circ \mathcal{Q}_{B \rightarrow R}$ implements a classical flip rule on each red site $i \in R$, conditional on the updated black configuration b' . Here, the bit $r_i \mapsto r'_i$ is flipped with probability

$$\Pr(r'_i = r_i \oplus 1 | b') = \sin^2(k_i(b')\theta), \quad \Pr(r'_i = r_i | b') = \cos^2(k_i(b')\theta), \quad (\text{C28})$$

Combining the two half-steps, the QCA update $\Delta_E \circ \mathcal{Q}$ under the system Pauli twirl induces the following step-step PCA kernel on configurations $s = (r, b) \mapsto s' = (r', b')$:

1. update $b \mapsto b'$ by flipping each $j \in B$ independently with probability $\sin^2(k_j(r)\theta)$;
2. update $r \mapsto r'$ by flipping each $i \in R$ independently with probability $\sin^2(k_i(b')\theta)$.

This is precisely the two-step PCA kernel defined in Section 7.2.

C.4 Conditional system Pauli emission

We now derive the induced system Pauli channel conditioned on the (updated) environment configuration.

Consider a single site and suppress the site index. Let $\tilde{\mathcal{U}}^{SE}$ be the twirled interaction from (A5), and define the reduced system channel

$$\mathcal{F}[\rho_S] := \text{Tr}_E(\tilde{\mathcal{U}}^{SE}[\rho_E \otimes \rho_S]). \quad (\text{C29})$$

From Sections C.2 and C.3, the environment state ρ_E entering the effective interaction is always a mixture of computational basis states. Inserting the Kraus representation from Eq. (C9),

$$\begin{aligned} \mathcal{F}[\rho_S] &= \sum_P \sum_{z, z'} \text{Tr}_S(K_{P,z}(\rho_E \otimes \rho_S)K_{P,z'}^\dagger) \\ &= \sum_P \sum_{z, z'} \frac{1}{4} \text{Tr}_S((\Pi_z \otimes PV_z P)(\rho_E \otimes \rho_S)(\Pi_{z'} \otimes PV_{z'} P)^\dagger) \\ &= \sum_{z, z'} \text{Tr}(\Pi_z \rho_E \Pi_{z'}) \cdot \frac{1}{4} \sum_P PV_z P \rho_S PV_{z'}^\dagger P. \end{aligned} \quad (\text{C30})$$

By the cyclicity of the trace and $\Pi_z \Pi_{z'} = \delta_{z, z'} \Pi_z$,

$$\mathcal{F}[\rho_S] = \sum_z \text{Tr}(\Pi_z \rho_E) \cdot \frac{1}{4} \sum_P PV_z P \rho_S PV_z^\dagger P, \quad (\text{C31})$$

with $\sum_z \text{Tr}(\Pi_z \rho_E) = 1$. As a result, \mathcal{F} is a convex combination of *conditional* system channels,

$$\mathcal{F}[\rho_S] = \sum_z p_z \mathcal{F}_z[\rho_S], \quad p_z := \text{Tr}(\Pi_z \rho_E), \quad \mathcal{F}_z[\rho_S] := \frac{1}{4} \sum_P PV_z P \rho_S PV_z^\dagger P. \quad (\text{C32})$$

For $z = 0, V_0 = I$, we immediately have

$$\mathcal{F}_0[\rho_S] = \rho_S. \quad (\text{C33})$$

For $z = 1, V_1 = \vec{n} \cdot \vec{\sigma}$, we observe that \mathcal{F}_1 is exactly the Pauli twirl of a unitary channel with single Kraus operator V_1 . The Pauli twirl of a channel with Kraus operators $\{K_i\}$ can be written as

$$\mathcal{T}_P(\mathcal{E})[\rho] = \frac{1}{d^2} \sum_P \sum_i |\text{Tr}(PK_i)|^2 P \rho P, \quad (\text{C34})$$

where d is the system dimension. Substituting $K_1 = V_1$ and $d = 2$ yields

$$\mathcal{F}_1[\rho_S] = \sum_P \frac{1}{4} |\text{Tr}(PV_1)|^2 P \rho_S P = \sum_P \frac{1}{4} |\text{Tr}(P(n_X X + n_Y Y + n_Z Z))|^2 P \rho_S P. \quad (\text{C35})$$

Using orthogonality of Pauli operators under the Hilbert-Schmidt inner product, we obtain the local system Pauli channel

$$\mathcal{F}_1[\rho_S] = n_X^2 X \rho_S X + n_Y^2 Y \rho_S Y + n_Z^2 Z \rho_S Z, \quad (\text{C36})$$

with $n_X^2 + n_Y^2 + n_Z^2 = 1$ by Eq. (C7).

For the full lattice, $U_{SE} = \bigotimes_{i \in V} U_{SE}^{(i)}$ and the twirl is applied locally, so conditional on the updated environment configuration $s_{t+1} \in \{0, 1\}^{|V|}$, the emitted Pauli string $x_t \in \{I, X, Y, Z\}^{|V|}$ factorises across sites with the above single-site channel.

C.5 Summary of full mapping

We now summarise the full mapping from the microscopic QCA noise model to the effective PCA HMM induced by the system Pauli twirl. We iterate through the PCA HMM steps as defined in Section 7.2, and justify each in reference to the assumptions and derivations throughout Sections C.1 to C.4.

0. **Environment initialisation.** Assumed in (A1), the initialisation is identical in both models.
1. **Storm update.** Assumed in (A2). The storm channel \mathcal{S}^E is only on the environment and preserves a diagonal ρ_E , so it is simulated exactly as a classical update on s_t and does not affect the subsequent reductions.
2. **PCA half-step (black).** By (A2)–(A3), the microscopic model applies $\mathcal{Q}_{R \rightarrow B}^E$. Under the twirl, Section C.2 dephases the environment in the computational basis, and Section C.3 shows $\Delta_B \circ \mathcal{Q}_{R \rightarrow B}^E$ is exactly the conditional independent flip update on B with probability $\sin^2(k\theta)$.
3. **PCA half-step (red).** Likewise, Section C.3 shows $\Delta_R \circ \mathcal{Q}_{B \rightarrow R}^E$ is exactly the conditional independent flip update on R with probability $\sin^2(k\theta)$, conditioned on the updated black configuration.
4. **Pauli emission.** By (A4)–(A5) and Section C.4, conditional on $s_{t+1}(i)$ the emitted Pauli is I if $s_{t+1}(i) = 0$, and $P \in \{X, Y, Z\}$ with probabilities n_P^2 if $s_{t+1}(i) = 1$, independently across sites.
5. **Repeat.** By (A2) and Section C.2, tracing out the system after the twirled interaction applies Δ_E , so the environment entering the next cycle is again diagonal; hence the above steps iterate cycle-by-cycle.

This completes the mapping from the microscopic QCA model in Section 7.1 to the effective PCA HMM in Section 7.2.